

Electronic Supplementary Information

Experimental Section

Materials: Juncus was obtained from the local Changsheng Pharmacy (Nanchang, China). Graphite felt (GF) was purchased from Beijing Jinglong Tetan Technology Co., Ltd. Sodium hydroxide (NaOH, 99.9%), ammonium chloride (NH₄Cl, 99.99%), ethanol (C₂H₆O, 99.0%), salicylic acid (C₇H₆O₃, 99.5%), sodium citrate dehydrate (C₆H₅Na₃O₇·2H₂O, 99.0%), p-dimethylaminobenzaldehyde (C₉H₁₁NO, 99.0%), sodium hypophosphite (NaH₂PO₂, 99%), sodium nitroferricyanide dihydrate (C₅FeN₆Na₂O·2H₂O, 99%), sodium nitrate (NaNO₃, 99.0%), sodium nitrite (NaNO₂, 99%), sodium dihydrogen phosphate dihydrate (NaH₂PO₄·2H₂O, 99.0%), disodium hydrogen phosphate dodecahydrate (Na₂HPO₄·12H₂O, 99%) Cobalt(II) acetate tetrahydrate and (Co(CH₃COO)₂·4H₂O, 99.9%), sodium hypochlorite solution (NaClO, Available chlorine ≥5.5%) were purchased from Aladdin Ltd. (Shanghai, China). Nitric acid (HNO₃, 65-68%), sulfuric acid (H₂SO₄, 98.3%), hydrogen peroxide (H₂O₂, 30 wt% in H₂O), hydrazine monohydrate (N₂H₄·H₂O, >98%), phosphoric acid (H₃PO₄, ≥85 wt% in H₂O), and ethyl alcohol (C₂H₅OH, 99.5%) were purchased from Beijing Chemical Corporation. The ultrapure water used throughout all experiments was purified through a Millipore system. All reagents were analytical reagent grade without further purification.

Synthesis of JDC: The Juncus was prewashed with distilled water under ultrasonic cleaning for 3 h, and then they were dried at 60 °C for 24 h under vacuum. The sample was calcinated at 800 °C for 2 h with a heating speed of 2 °C min⁻¹ in Ar atmosphere. Lastly, the JDC was collected after cooled to ambient temperature under Ar.

Synthesis of Co@JDC: The Juncus was prewashed with distilled water under ultrasonic cleaning for 3 h, and then they were dried at 60 °C for 24 h. After that, 0.15 g Juncus was added into 40 mL 0.1 M Co(CH₃COO)₂·4H₂O solution for 24 h and dried at 60 °C for another 24 h under vacuum. Subsequently, this sample was annealed at 800 °C with a heating speed of 2 °C min⁻¹ for 2 h in Ar atmosphere.

Lastly, the Co@JDC was collected after cooled to ambient temperature under Ar.

Characterization:

X-ray diffraction (XRD) analysis was performed with a Haoyuan DX-2700BH diffractometer. Copper $K\alpha$ radiation (1.54 Å) was generated with a tube voltage of 40 kV and a tube current of 30 mA. The incident beam was focused with a diameter mono-capillary collimator. An aligned laser beam was used to ensure that the sample was placed at the correct depth for diffraction measurements. Coupled theta/two theta mode was used, with a θ angle that was half of the 2θ angle. The scattered x-ray radiation was collected by the detector with an angular resolution $< 0.02^\circ$. One scan was performed in the range of 10° to 80° , and radiation was counted for a total duration of 1 h to obtain the XRD profile. The collected data were analyzed using Jade 6.5 software.

Scanning electron microscopy (SEM) and energy dispersive X-ray (EDX) elemental mapping images were collected on a Gemini SEM 300 scanning electron microscope (ZEISS, Germany) at an accelerating voltage of 5 kV.

Transmission electron microscopy (TEM) images were obtained from a Zeiss Libra 200FE transmission electron microscope operated at 200 kV. After ultrasonic dispersion of the samples for 20 min, the samples were prepared using a double membrane.

N_2 adsorption/desorption tests (Micromeritics ASAP 2460) were done to probe the porosity and specific area of the Co@JDC. Before analysis, the samples were degassed at 120°C for 12 h under vacuum. The specific surface area was calculated based on nitrogen adsorption isotherms by Brunauer-Emmett-Teller (BET) analysis. The pore size distribution was calculated by non-local density functional theory (NLDFT) methods via the desorption branch. The N_2 gas sorption isotherm was measured at 77 K.

The weight content of Co element in Co@JDC was determined by an inductively coupled plasma-optical emission spectrometry (ICP-OES, Agilent 5110, Agilent, USA) after concentrated acids ($\text{HNO}_3:\text{H}_2\text{O}_2 = 7:1$, v/v) digestion.

Absorbance data were acquired on SHIMADZU UV-2700 Ultraviolet-visible

(UV-Vis) spectrophotometer. All electrolytes were calibrated by the spectrophotometric method. Detailed procedures for the detection of NH_3 , N_2H_4 , and NO_2^- are presented below.

Determination of NH_3 : NH_3 concentration was spectrophotometrically determined by the indophenol blue method.⁴ In a typical colorimetric assay, 2 mL of the catholyte after electrolysis were mixed with 1 mL of NaClO solution (4.5%), 2 mL of 1 M NaOH solution (5% $\text{C}_7\text{H}_6\text{O}_3$ and 5% $\text{C}_6\text{H}_5\text{Na}_3\text{O}_7 \cdot 2\text{H}_2\text{O}$), and 0.2 mL of mixed solution (1 g $\text{Na}_2\text{Fe}(\text{CN})_5\text{NO} \cdot 2\text{H}_2\text{O}$ diluted to 100 mL with ultrapure water). Absorbance measurements were performed at $\lambda = 655$ nm. The concentration absorbance curves were calibrated using the standard NH_4Cl solution with different NH_3 concentrations in 0.1 M NaOH/0.1 M PBS.

Determination of N_2H_4 : The generated N_2H_4 during bulk electrolysis was detected using the method of Watt and Chrisp.⁵ The color reagent is composed of a mixed solution of $\text{C}_9\text{H}_{11}\text{NO}$ (5.99 g), HCl (30 mL), and $\text{C}_2\text{H}_5\text{OH}$ (300 mL). 5 mL of the collected electrolyte after electrocatalytic tests were added into 5 mL of the above color reagent, and kept stirring for 15 min at 25 °C, which were measured at the absorbance of 455 nm then. The concentration absorbance curves were calibrated using the standard $\text{N}_2\text{H}_4 \cdot \text{H}_2\text{O}$ solution with different N_2H_4 concentrations in 0.1 M NaOH/0.1 M PBS.

Determination of NO_2^- : Griess tests can be applied to determine the remaining NO_2^- concentration in the reaction electrolytes.⁶ Firstly, the Griess reagents were prepared by dissolving 0.2 g N-(1-naphthyl) ethylenediamine dihydrochloride, 2.0 g sulfonamide, and 5.88 mL H_3PO_4 in 100 mL ultrapure water. Then, diluting the electrolyte to a measurable concentration range. After that, 1.0 mL of the tested electrolyte was added in to a mixture of 1.0 mL of Griess eagent and 2.0 mL ultrapure water to react at room temperature for 10 min under dark conditions, where an azo dye (magenta) can be formed. Absorbance for such colored solutions at the absorbance of 540 nm was recorded for the yields quantification. The concentration absorbance curves were calibrated using the standard NaNO_2 solution with different NO_2^- concentrations in 0.1 M NaOH/0.1 M PBS.

Gaseous products from nitrate/nitrite reduction reaction were determined by GC with SHIMADZU GC-2014 gas chromatograph. The electrolyzer outlet was introduced into a condenser before being vented directly into the gas-sampling loop of the gas chromatograph. A GC run was initiated every 1200 s. Argon (99.999%) was used as the carrier gas. A flame ionization detector with a thermal conductivity detector (TCD) was used to quantify hydrogen and nitrogen.

Electrochemical measurements: 10 mg of the catalyst and 40 μL of 5 wt% Nafion were dispersed in 960 μL of a deionized water/ethanol solution (v/v = 1:3) by sonicating for 2 h to get a homogeneous catalyst ink. Then, a certain volume of the ink was dropped onto a 1×1 cm graphite felt mesh with a catalyst loading of 1.0 mg cm^{-2} and dried at $80 \text{ }^\circ\text{C}$ for 2 h. The electrocatalytic measurements, including the LSV curves, were carried out using a typical H-cell separated by a clean piece of Nafion 117 membrane under ambient conditions (using CHI 660E electrochemical analyzer). The membrane was protonated with boiled water, H_2O_2 (5%) solution, as well as 0.5 M H_2SO_4 , successively. Electrochemistry NO_2RR and NO_3RR tests were carried out in 0.1 M PBS (PH = 7) solution with 0.1 M NO_2^- or 0.1 M NO_3^- using a three-electrode configuration consisting of Co@JDC ($0.5 \text{ cm} \times 0.5 \text{ cm}$), Ag/AgCl reference electrode, and graphite rod (6.0 mm in diameter) counter electrode. Electrochemistry NO_2RR and NO_3RR tests were carried out in 0.1 M NaOH (PH = 13) solution with 0.1 M NO_2^- or 0.1 M NO_3^- using a three-electrode configuration consisting of Co@JDC ($0.5 \text{ cm} \times 0.5 \text{ cm}$), Hg/HgO reference electrode, and graphite rod (6.0 mm in diameter) counter electrode. Current densities in this report was recorded and normalized to the geometric area of different working electrodes. The typical concentrations of nitrite in nuclear waste was about 0.6 M^1 and the average concentration of nitrite in the groundwater was about 0.5 mg/L^2 .

The key experiments were repeated 2 to 3 times using the same electrode in order to confirm the electrode stability and the reproducibility of results.

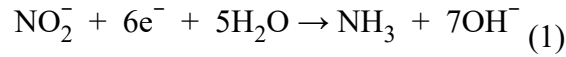
RHE calibration: The reference electrodes were calibrated with respect to reversible hydrogen electrode (RHE).³ The calibration was performed in the high purity hydrogen saturated electrolyte with a platinum foil (1 cm^2) as the working electrode.

CVs were run at a scan rate of 1 mV s⁻¹, and the average of the two potentials at which the current crossed zero was taken to be the thermodynamic potential for the hydrogen electrode reactions. In all measurements, Hg/HgO and Ag/AgCl electrodes were calibrated to RHE if there are no special notes as following: So in 0.1 M NaOH, E (vs. RHE) = E (vs. Hg/HgO) + 0.867 V. In 0.1 M PBS, E (vs. RHE) = E (vs. Ag/AgCl) + 0.605 V (Fig. S4).

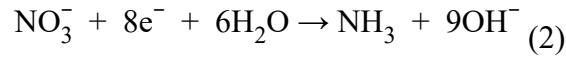
Determination of H₂ and N₂: H₂ and N₂ was monitored by gas chromatography (GC).

Determination of FE and NH₃ yield:

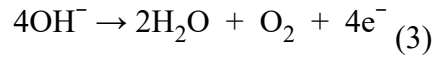
Equations of cathode reaction of NO₂RR in neutral/alkaline media:



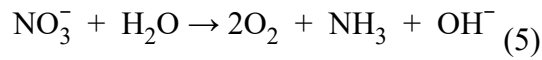
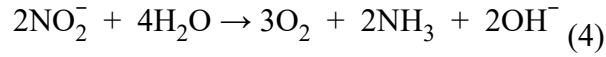
Equations of cathode reaction of NO₃RR in neutral/alkaline media:



Equations of anode reaction:



Possible overall reaction of NO₂RR and NO₃RR:



FE toward NH₃ via NO₂RR was calculated by equation:

$$\text{FE} = 6 \times F \times \left([\text{NH}_3] \times \frac{V}{M_{\text{NH}_3}} \right) / Q \times 100\% \quad (6)$$

FE toward NH₃ via NO₃RR was calculated by equation:

$$\text{FE} = 8 \times F \times \left([\text{NH}_3] \times \frac{V}{M_{\text{NH}_3}} \right) / Q \times 100\% \quad (7)$$

NH₃ yield was calculated using the following equation:

$$\text{NH}_3 \text{ yield} = [\text{NH}_3] \times \frac{V}{(M_{\text{NH}_3} \times t \times A)} \quad (8)$$

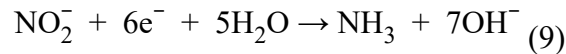
Where 6 and 8 are electron transfer numbers for NO₂RR and NO₃RR, respectively (the reduction of NO₂⁻ to NH₃ consumes 6 electrons, and the reduction of NO₃⁻ to

NH₃ consumes 8 electrons), F is the Faradic constant (96500 C mol⁻¹), M_{NH_3} is the molar mass of NH₃ (M = 17), [NH₃] is the measured NH₃ concentration (The unit of [NH₃] is mg L⁻¹), V is the volume of electrolyte in the cathodic or anodic compartment (50 mL), the unit of V is L, Q is the total quantity of applied electricity; t is the reduction time (1 h), and A is the geometric area of working electrode (0.5 × 0.5 cm²).

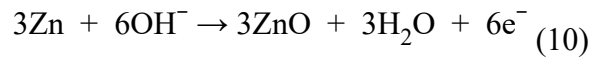
Assembly of the zinc-NO₂⁻ (NO₃⁻) battery and electrochemical test: The Co@JDC/GF (0.5 × 0.5 cm²) electrode was employed as the cathode to perform the NO₂RR or NO₃RR in a cathodic electrolyte (50 mL 0.1 M NaOH + 0.1 M NaNO₂ or NaNO₃). A polished Zn plate (1 × 1 cm²) was set in an anodic electrolyte (50 mL 1 M NaOH), and a bipolar membrane was used to separate the two different electrolytes. During, the Zn-NO₂⁻ (NO₃⁻) electrochemistry implements electrochemical NO₂⁻ or NO₃⁻ reduction driven by Zn dissolution. The discharging polarization curves with a scan rate of 5 mV/s and galvanostatic tests were conducted using CHI 660E workstation at room temperature, respectively. The power density (P) of zinc-nitrate battery was determined by P = I × V, where I and V are the discharge current density and voltage, respectively.

The electrochemical reactions in Zn-NO₂⁻ battery are presented as following:

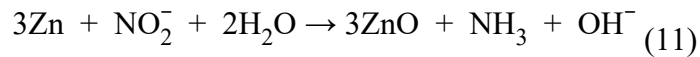
Cathode reaction:



Anode reaction:

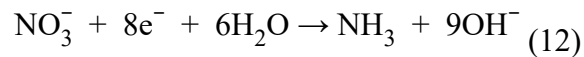


Overall reaction:

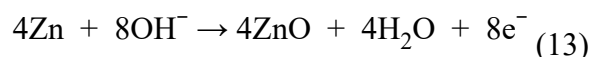


The electrochemical reactions in Zn-NO₃⁻ battery are presented as following:

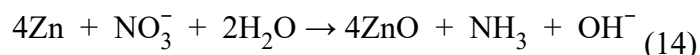
Cathode reaction:



Anode reaction:



Overall reaction:



Solar cell testing: For the photovoltaic-electrolysis experiments, a solar cell was coupled to a 2-electrode H-type cell.⁷ A Xenon lamp solar simulator (PLS-SXE300, Perfectlight) equipped reproduce an AM1.5G illumination (100 mW cm⁻²). The optical power was measured by an optical power meter (PLS-MW2000, Perfectlight).

PV-electrolysis measurements: A solar panel (CNC 40X220-18, AZAVA) as a power source tandem with an H-type cell to drive NO₂RR. The light source was a 300 W xenon lamp (PLS-SXE300, Perfectlight). The optical power of the sun was measured by an optical power meter (PLS-MW2000, Perfectlight).

Computational Details:

Methods: All calculations were performed using the plane wave based periodic DFT method as implemented in the Vienna Ab Initio Simulation Package (VASP).^{8,9} The electron-ion interaction was described with the projector augmented wave (PAW) method.^{10,11} The electron exchange and correlation energies were treated within the generalized gradient approximation in the Perdew-Burke-Ernzerhof functional (GGA-PBE).¹² The plane wave basis was set up to 400 eV. Electron smearing was used via the Methfessel-Paxton technique with a smearing width consistent to $\sigma = 0.2$ eV.

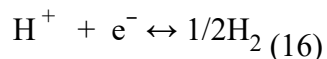
The adsorption energy was calculated according to $E_{\text{ads}} = E_{\text{X/slab}} - [E_{\text{slab}} + E_{\text{X}}]$, where $E_{\text{X/slab}}$ is the total energy of the slab with adsorbates in its equilibrium geometry, E_{slab} is the total energy of the bare slab, and E_{X} is the total energy of the free adsorbates in the gas phase. Therefore, the more negative the E_{ads} , the stronger the adsorption.

The Gibbs free energy change (ΔG) for each gaseous and adsorbed species were calculated by Equation. 15:

$$\Delta G = E_{\text{ads}} + E_{\text{ZPE}} - TS \quad (15)$$

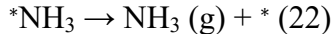
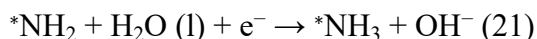
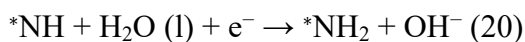
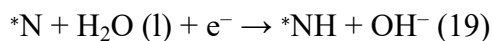
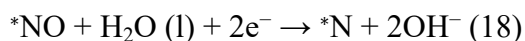
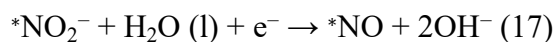
where E_{ZPE} is zero-point energy calculated with VASP, TS is the entropy contribution at 298.15 K. Computational hydrogen electrode (CHE) model proposed by Nørskov et

al was used to calculate the free energy change of each reaction step that involves an electrochemical proton-electron transfer. In this model, zero voltage is defined based on the reversible hydrogen electrode (RHE), in which the reaction:



is defined to be in equilibrium at zero voltage, at all values of pH, at all temperatures, and with H₂ at 101325 Pa pressure. Therefore, the free energy of a proton-electron pair $\Delta G_{(\text{H}^+ + \text{e}^-)}$ is equal to half of the free energy of gaseous hydrogen ($1/2 \Delta G_{\text{H}_2}$) at a potential of 0 V.

The NO₂⁻ reduction reactions were simulated as follows:



Models: In Fig. S36, the calculated lattice constant of Co is $a = b = c = 3.51637 \text{ \AA}$ and $\alpha = \beta = \gamma = 90^\circ$. The top and side view of three catalyst models of Co(111), Co(200) and Co(220) were shown, in which the unit cell $p(3 \times 3)$, $p(3 \times 3)$, and $p(3 \times 2)$, as well as the $3 \times 3 \times 1$ k-point sampling are chosen for these three models. Totally, the Co(111) and Co(200) has 36 Co atoms, in which 9 Co atoms were fixed; the Co(220) has 42 Co atoms, in which 13 Co atoms were fixed.

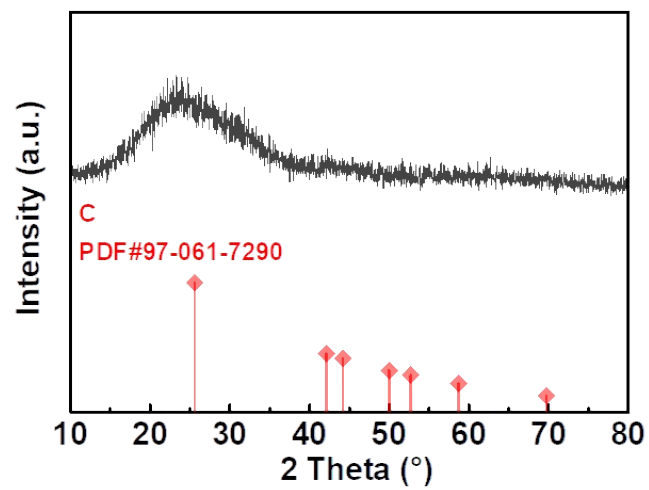


Fig. S1. XRD pattern of JDC.

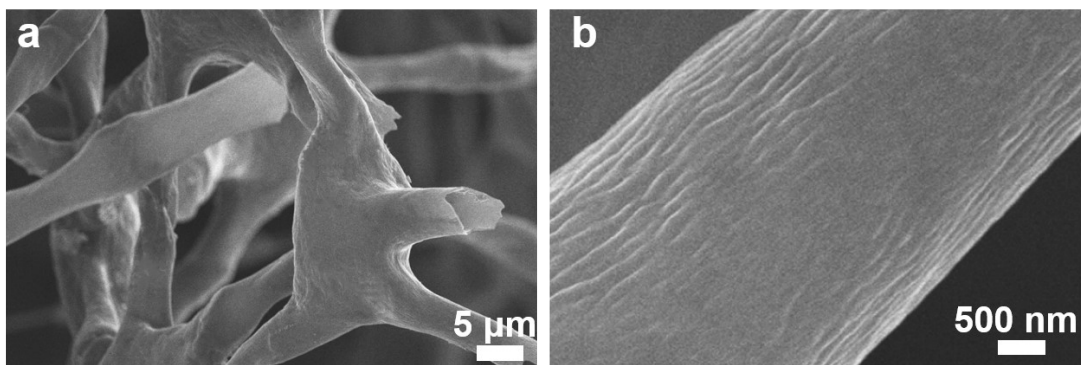


Fig. S2. (a) and (b) SEM images of JDC.

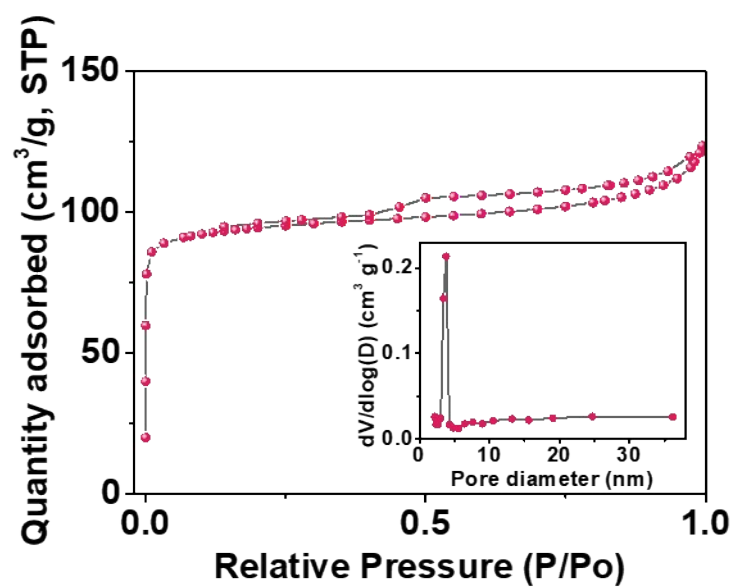


Fig. S3. The typical nitrogen adsorption-desorption isotherm and the corresponding BJH pore size of the Co@JDC.

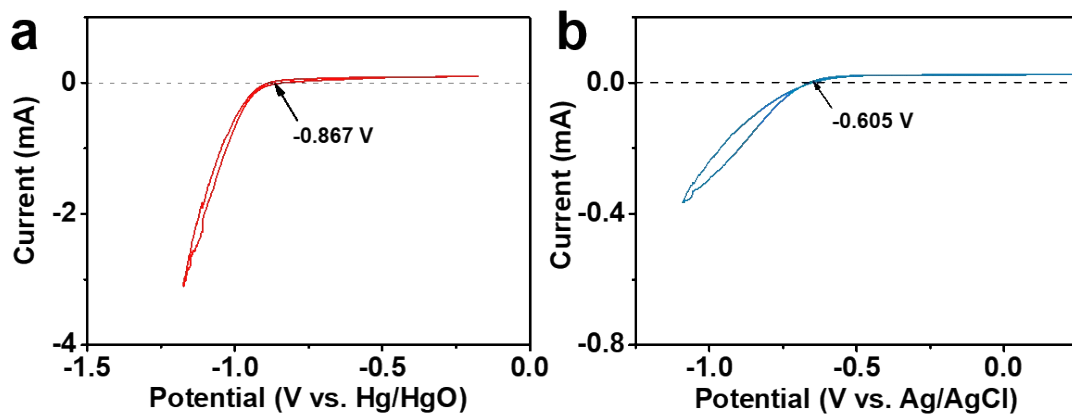


Fig. S4. (a) The Hg/HgO/1 M KOH reference electrode was calibrated with respect to RHE in 0.1 M NaOH. (b) The Ag/AgCl/saturated KCl reference electrode was calibrated with respect to RHE in 0.1 M PBS. Based on the calibrated, we have:
 in 0.1 M NaOH, $E (\text{vs. RHE}) = E (\text{vs. Hg/HgO}) + 0.867 \text{ V}$;
 in 0.1 M PBS, $E (\text{vs. RHE}) = E (\text{vs. Ag/AgCl}) + 0.605 \text{ V}$.

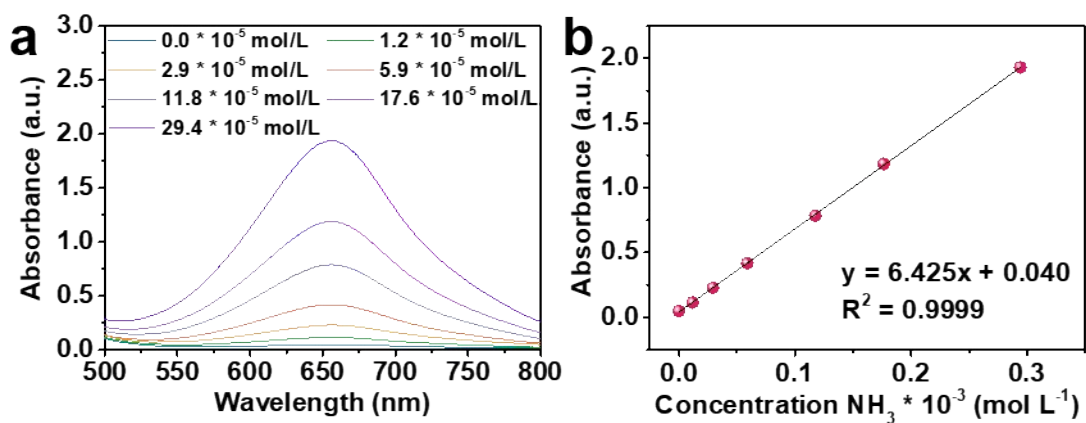


Fig. S5. (a) UV-Vis adsorption spectra of standard solution with different concentrations of NH_3 in 0.1 M NaOH. (b) Linear standard plot to determine NH_3 yields in 0.1 M NaOH.

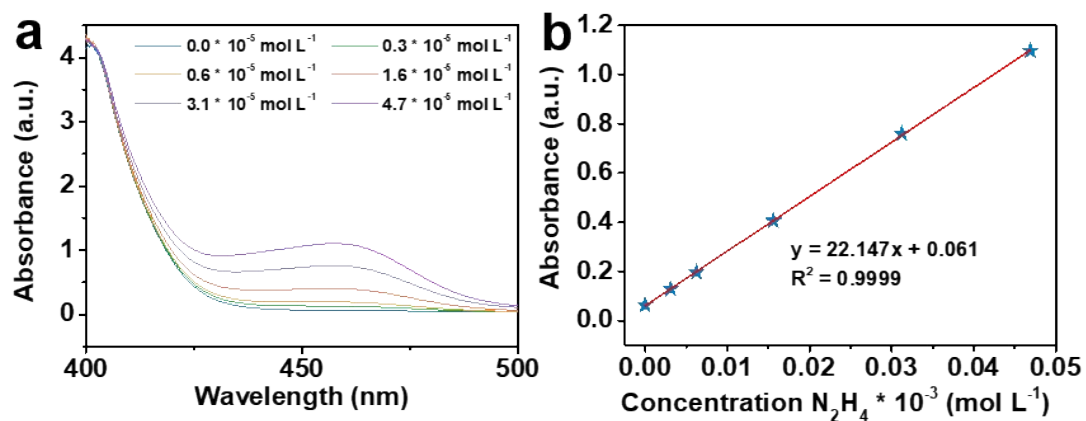


Fig. S6 (a) UV-Vis adsorption spectra of standard solution with different concentrations of N_2H_4 in 0.1 M NaOH. (b) Linear standard plot to determine N_2H_4 yields in 0.1 M NaOH.

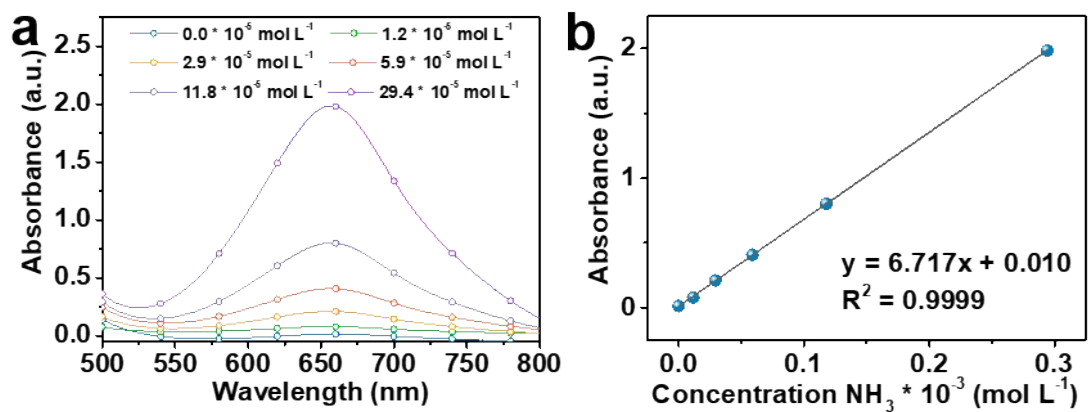


Fig. S7. (a) UV-Vis adsorption spectra of standard solution with different concentrations of NH_3 in 0.1 M PBS. (b) Linear standard plot to determine NH_3 yields in 0.1 M PBS.

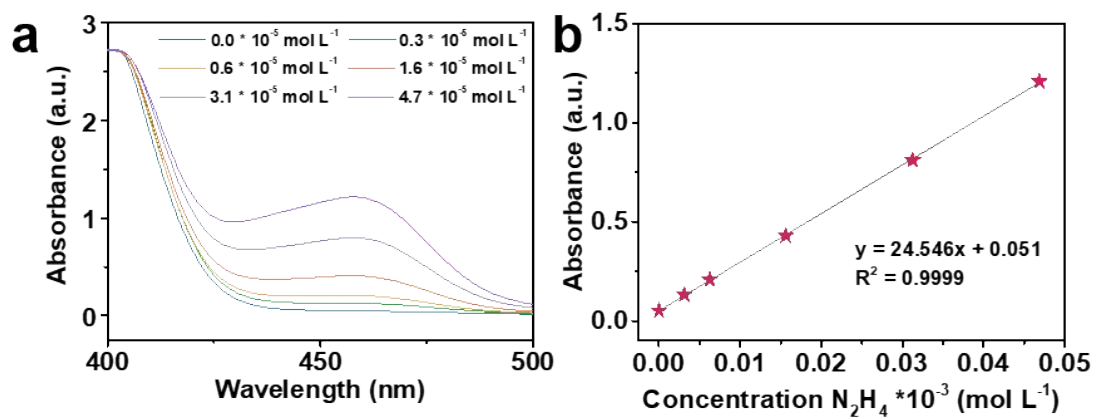


Fig. S8. (a) UV-Vis adsorption spectra of standard solution with different concentrations of N_2H_4 in 0.1 M PBS. (b) Linear standard plot to determine N_2H_4 yields in 0.1 M PBS.

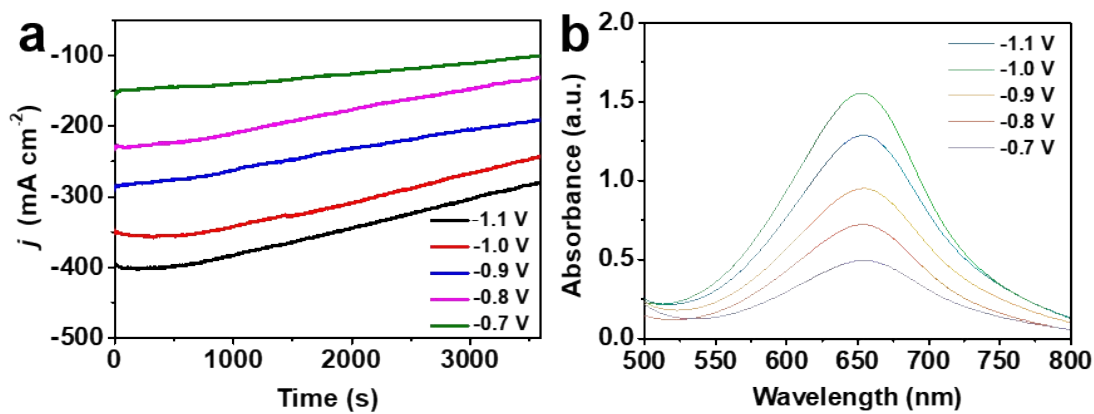


Fig. S9. (a) Chronoamperometry curves of the Co@JDC/GF electrode for electrocatalytic NO₂RR at different potentials in 0.1 M NaOH electrolyte with 0.1 M NO₂⁻. (b) UV-Vis adsorption spectra of the electrolytes with 50 times dilution after 1 h NO₂RR electrolysis on Co@JDC/GF at different potentials.

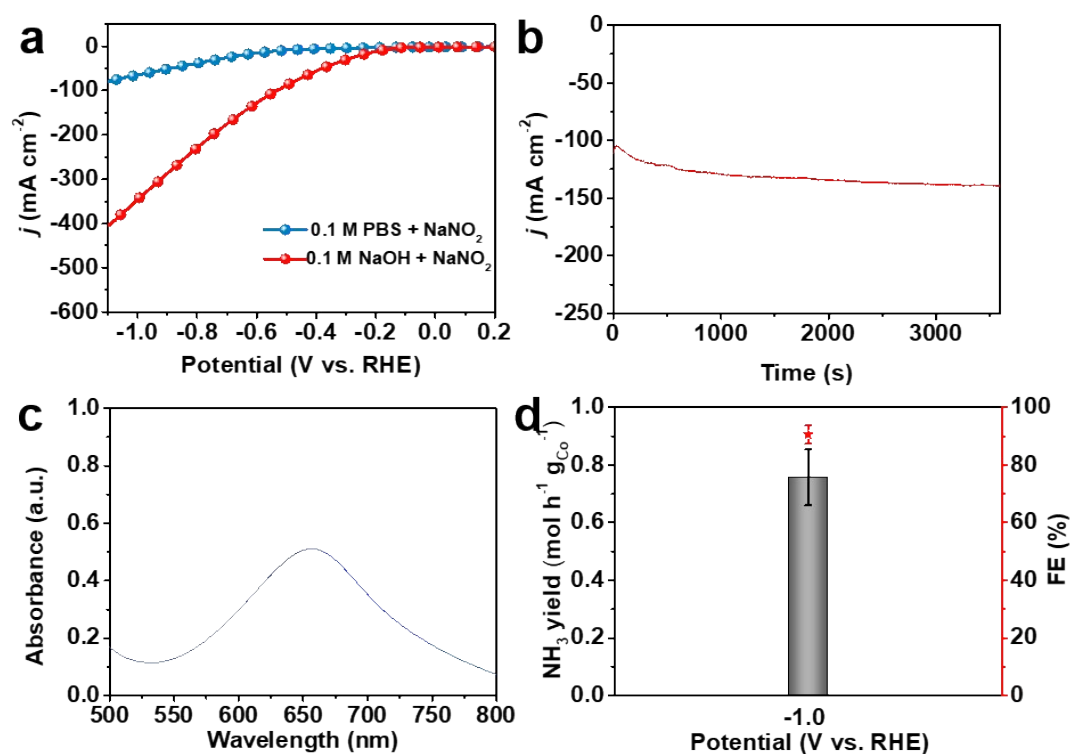


Fig. S10. (a) LSV curves of Co@JDC/GF for NO₂RR in 0.1 M PBS or 0.1 M NaOH electrolyte with 0.1 M NO₂⁻ at a scan rate of 5mV s⁻¹ from 0.2 V to -1.1 V. (b) Chronoamperometry curve and (c) UV-Vis adsorption spectrum of the electrolyte with 50 times dilution after 1 h NO₂RR electrolysis on Co@JDC/GF at -1.0 V in 0.1 M PBS with 0.1 M NO₂⁻. (d) Corresponding NH₃ yield and FE of the Co@JDC/GF electrode at -1.0 V. The error bars correspond to the standard deviations of measurements over three separately prepared samples under the same conditions.

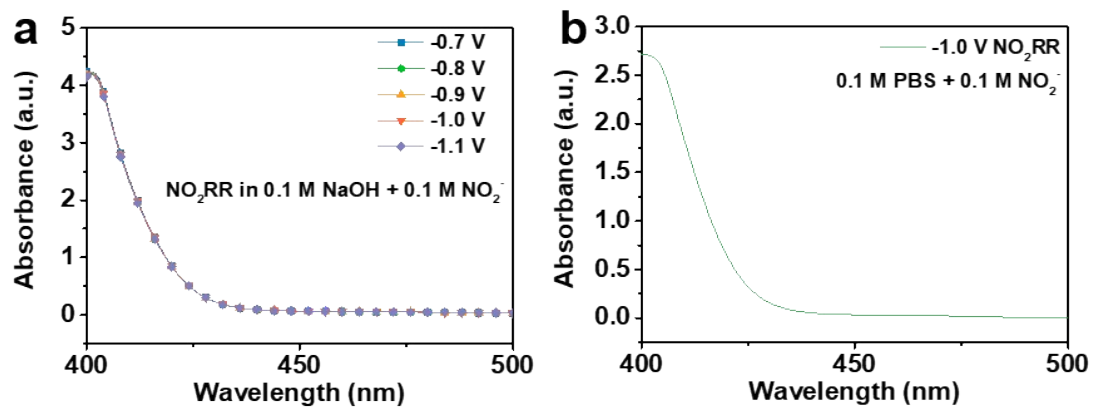


Fig. S11. (a) UV-Vis adsorption spectra of N_2H_4 in the alkaline electrolyte after electrocatalytic NO_2RR . (b) UV-Vis adsorption spectrum of N_2H_4 in the neutral electrolyte after electrocatalytic NO_2RR . There was no generation of N_2H_4 in the process of electrocatalytic NO_2RR .

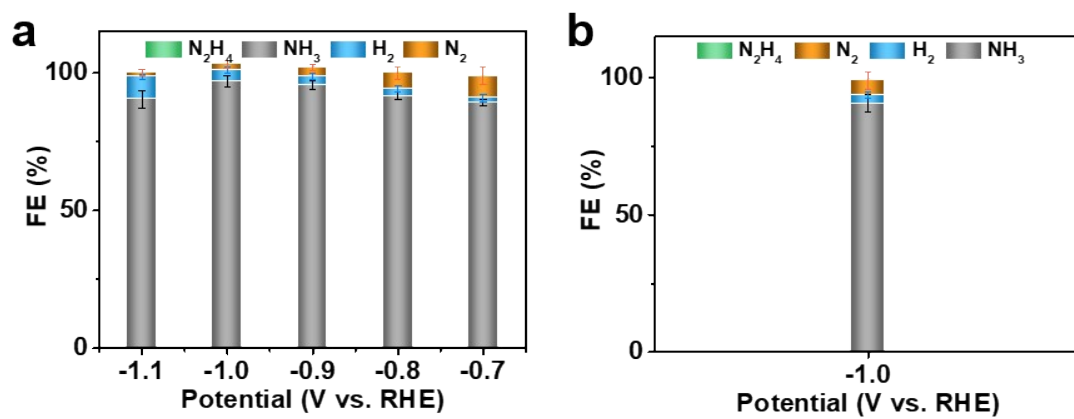


Fig. S12. (a) Product distribution for NO₂RR in the alkaline electrolyte at different potentials. (b) Product distribution for NO₂RR in the neutral electrolyte at -1.0 V. The error bars correspond to the standard deviations of measurements over three separately prepared samples under the same conditions.

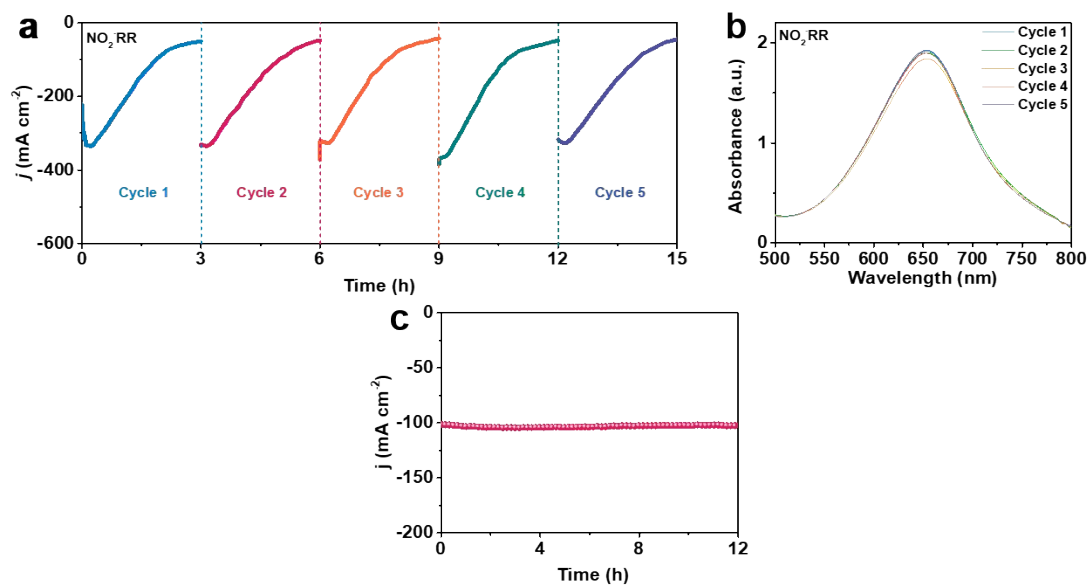


Fig. S13. (a) Stability measurement of Co@JDC/GF in 0.1 M NaOH with 0.1 M NO₂⁻ (with refreshing the electrolytes) at a fixed potential of -1.0 V. (b) UV-Vis adsorption spectra of the electrolyte with 50 times dilution after NO₂RR electrolysis on Co@JDC/GF. (c) Long-term stability tests for Co@JDC/GF in 0.1 M NaOH with 0.1 M NO₂⁻ at -0.3 V.

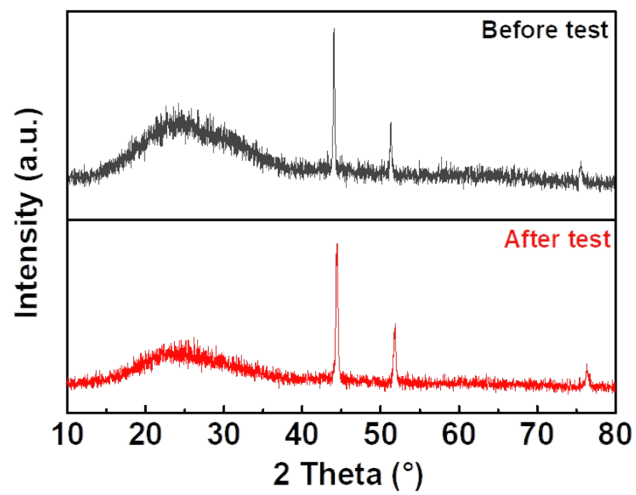


Fig. S14. XRD patterns of Co@JDC before and after the cycling test.

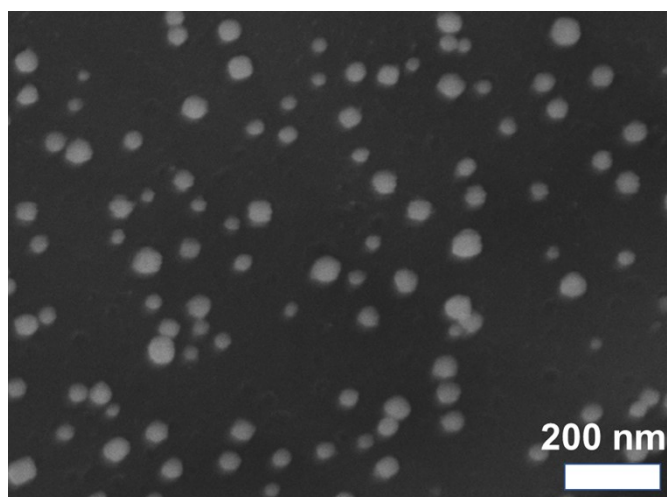


Fig. S15. SEM image of Co@JDC after the cycling test.

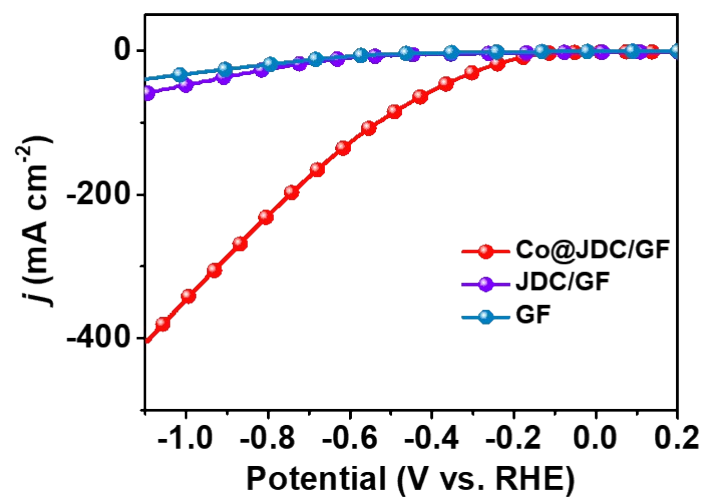


Fig. S16. LSV curves of Co@JDC/GF, JDC/GF, and GF for NO₂RR in 0.1 M NaOH with 0.1 M NO₂⁻ at a scan rate of 5 mV s⁻¹ from 0.2 V to -1.1 V.

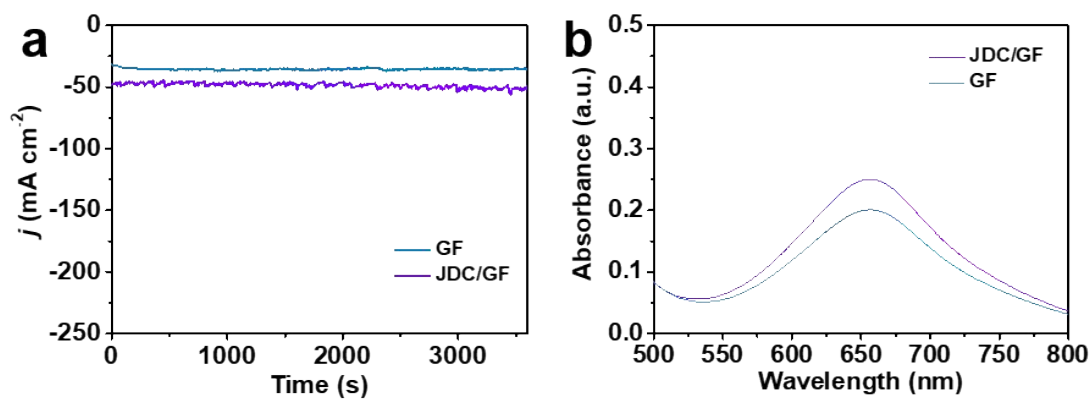


Fig. S17. (a) Chronoamperometry curves and (b) UV-Vis adsorption spectra of the electrolyte with 10 times dilution after 1 h NO₂RR electrolysis on JDC/GF and GF at -1.0 V in 0.1 M NaOH with 0.1 M NO₂⁻.

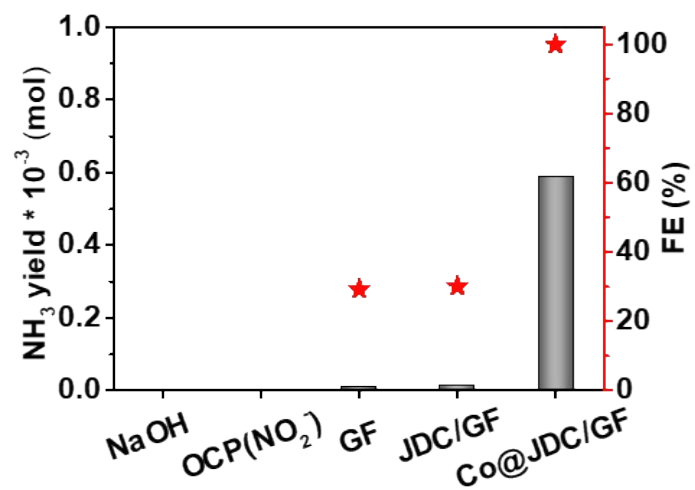


Fig. S18. Comparison of NH₃ yields after 1h electrolysis of different electrocatalysts.

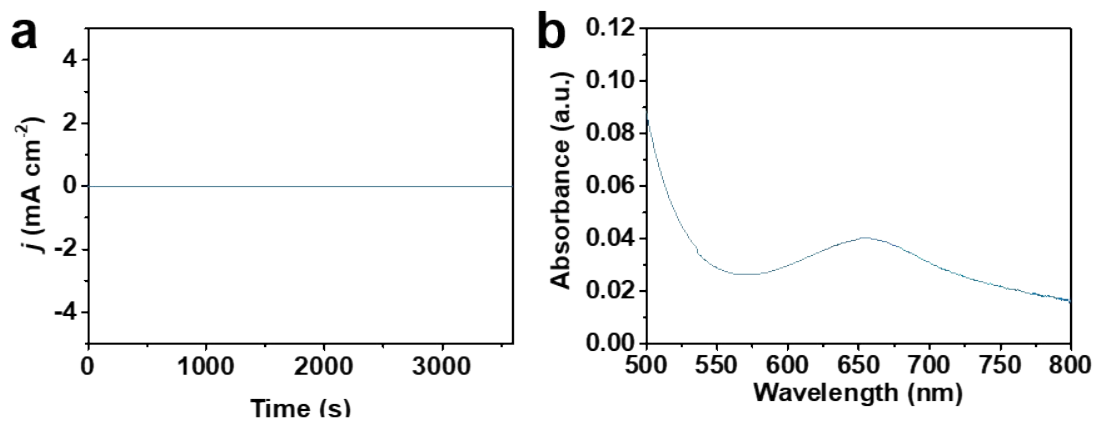


Fig. S19. (a) Chronoamperometry curve and (b) UV-Vis adsorption spectrum of the electrolyte after 1 h electrolysis on Co@JDC/GF at OCP in 0.1 M NaOH with 0.1 M NO_2^- .

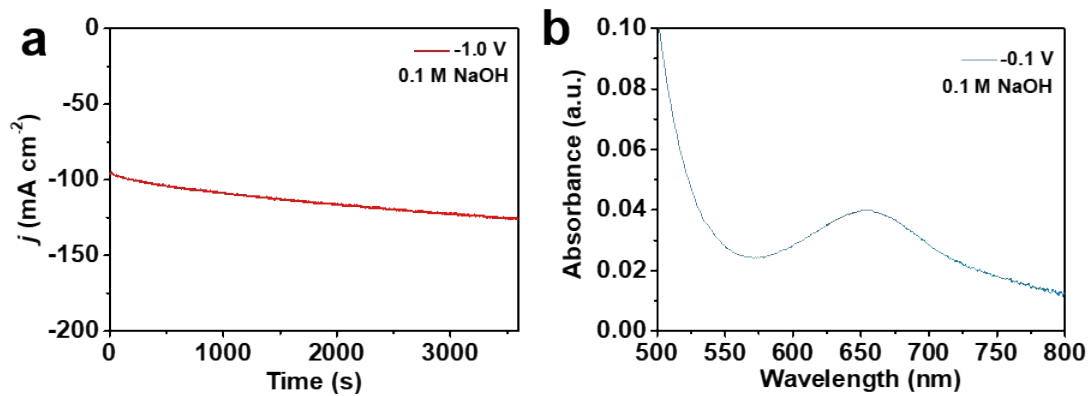


Fig. S20. (a) Chronoamperometry curve and (b) UV-Vis adsorption spectrum of the electrolyte after 1 h electrolysis on Co@JDC/GF at -1.0 V in 0.1 M NaOH.

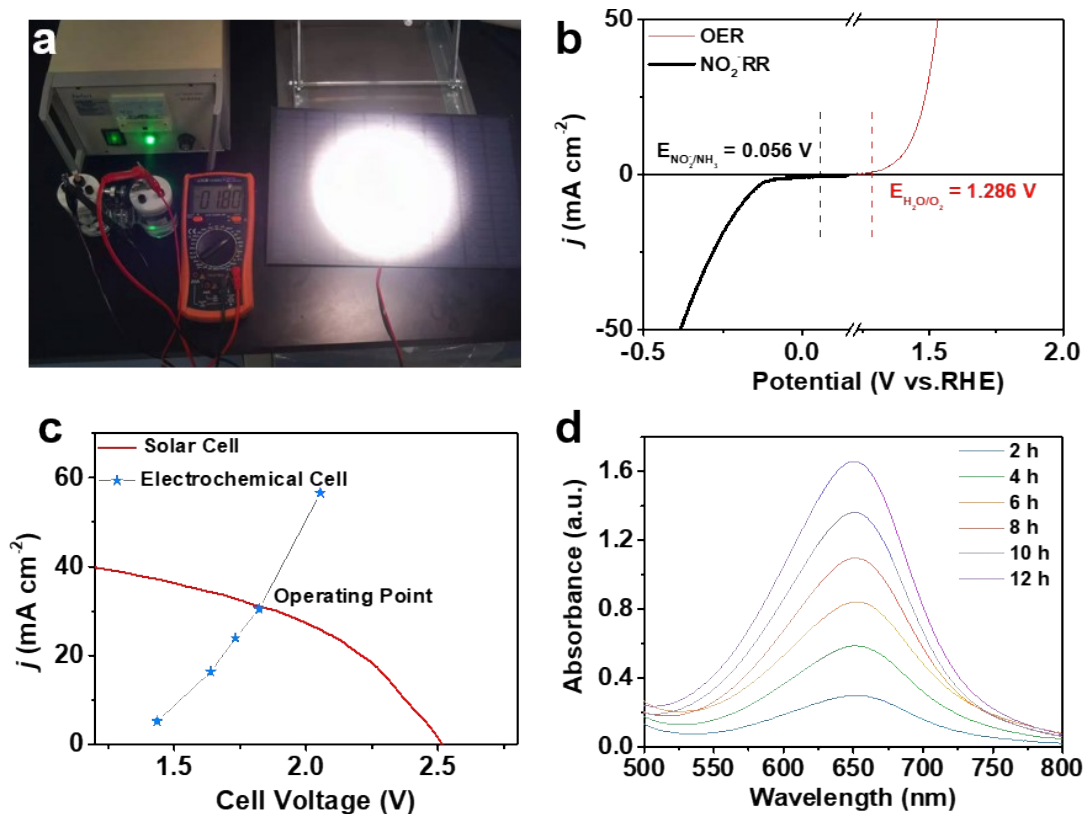


Fig. S21. (a) Schematic of PV-electrolyzer system for solar-driven NH_3 synthesis. (b) LSV curves of Co@JDC/GF . The LSV responses were measured in a 3-electrode configuration at a scan rate of 5 mV s^{-1} (scan range of cathode is from 0.2 V to -1.1 V and range of anode is from 1.0 V to 1.8 V). (c) Intersection of j -V characteristics of Co@JDC/GF triple-junction solar cell at 1 sun of AM1.5G irradiance with the load curve of an electrochemical cell. The operating current is 30 mA and the potential is 1.8 V. (d) UV-Vis adsorption spectra of the electrolyte with 10 times dilution after electrolysis on Co@JDC/GF under different time periods for the solar cell system.

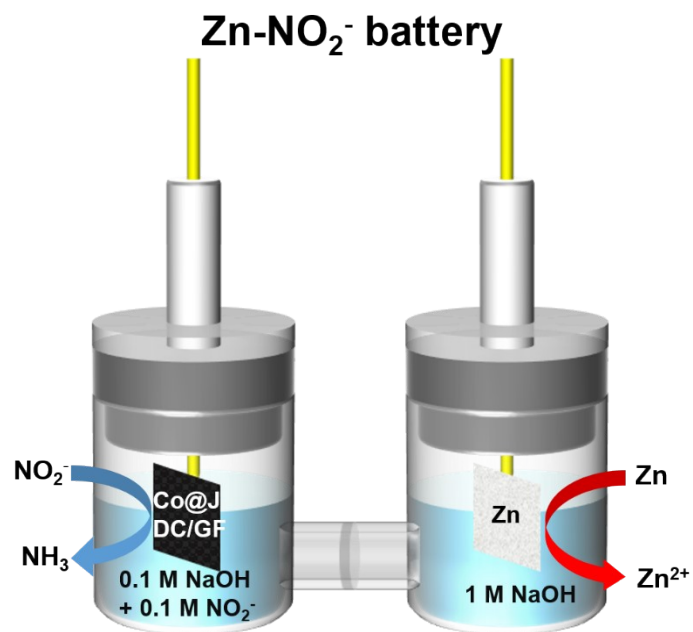


Fig. S22. Schematic of the zinc-NO₂⁻ battery.

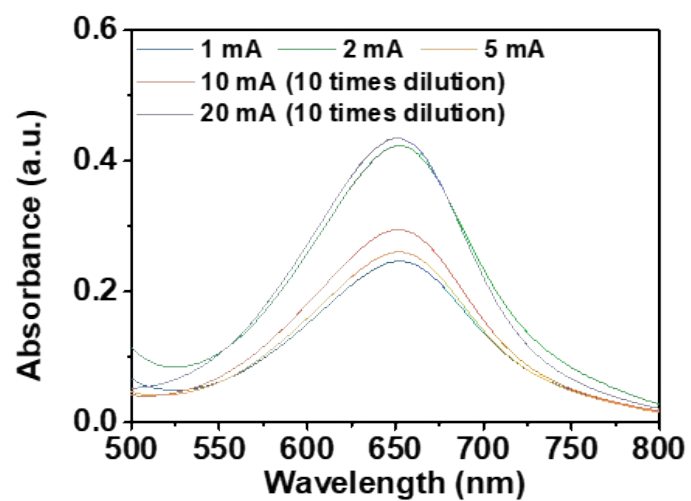


Fig. S23. UV-Vis adsorption spectra of NH₃ for the Zn-NO₂⁻ battery system at different current densities.

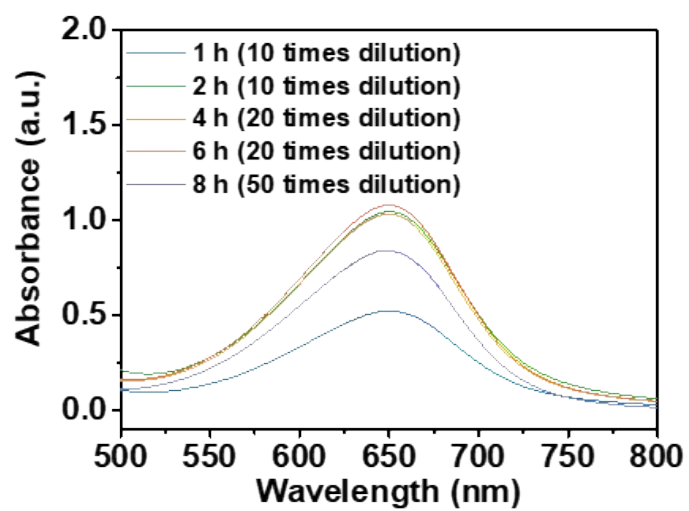


Fig. S24. UV-Vis adsorption spectra of NH₃ under different time periods for the Zn-NO₂⁻ battery system.

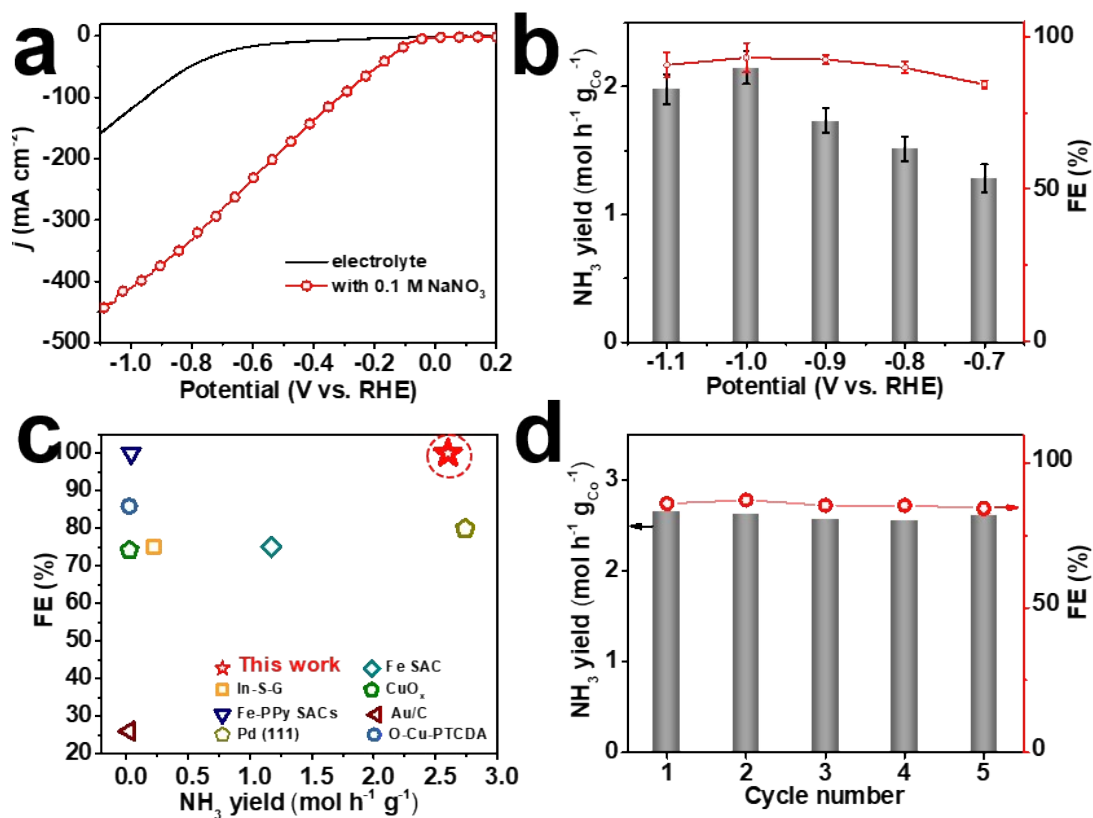


Fig. S25. (a) LSV curves of the Co@JDC/GF in 0.1 M NaOH electrolytes with and without 0.1 M NO₃⁻ at a scan rate of 5 mV s⁻¹ from 0.2 V to -1.1 V. (b) FEs and NH₃ yields of Co@JDC/GF. The error bars correspond to the standard deviations of measurements over three separately prepared samples under the same conditions. (c) Comparing NH₃ yields and FEs of Co@JDC/GF with recent NO₃RR catalysts. (d) Cycling tests.

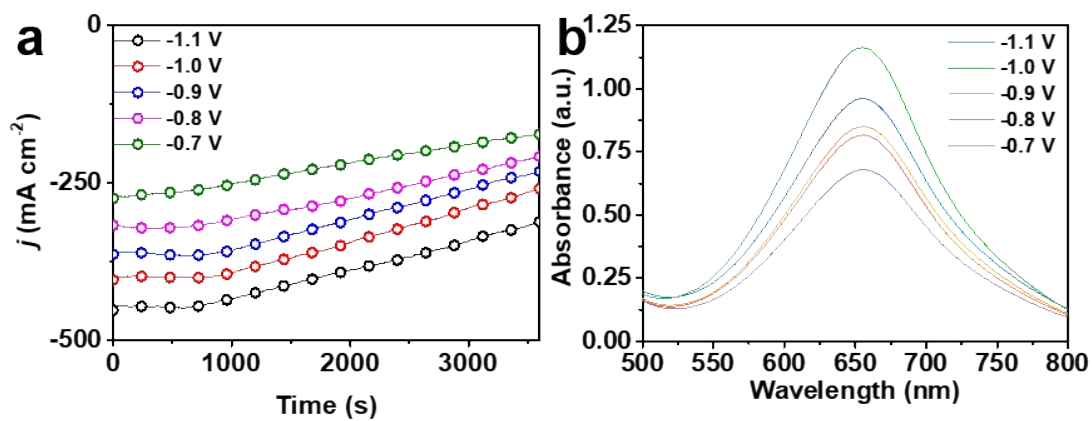


Fig. S26. (a) Chronoamperometry curves of the Co@JDC/GF electrode for electrocatalytic NO₃RR at different applied potentials in 0.1 M NaOH electrolyte with 0.1 M NO₃⁻. (b) UV-Vis adsorption spectra of electrolytes with 50 times dilution after electrolysis on Co@JDC/GF at different potentials in 0.1 M NaOH with 0.1 M NO₃⁻.

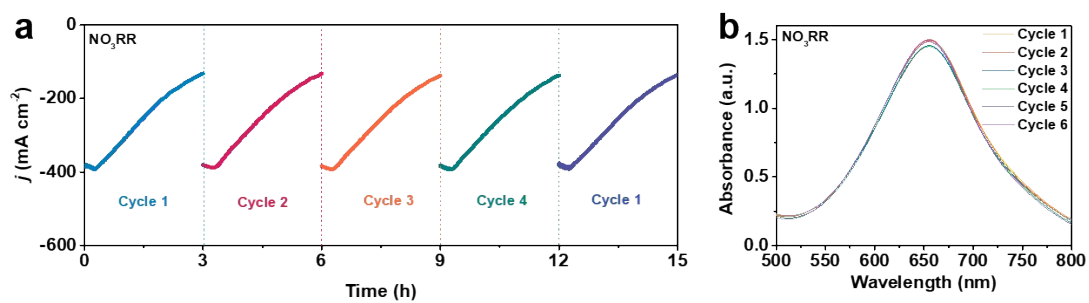


Fig. S27. (a) Stability measurement of Co@JDC/GF in 0.1 M NaOH with 0.1 M NO₃⁻ (with refreshing the electrolytes) at a fixed potential of -1.0 V. (b) UV-Vis adsorption spectra of electrolytes with 50 times dilution after electrolysis on Co@JDC/GF in 0.1 M NaOH with 0.1 M NO₃⁻.

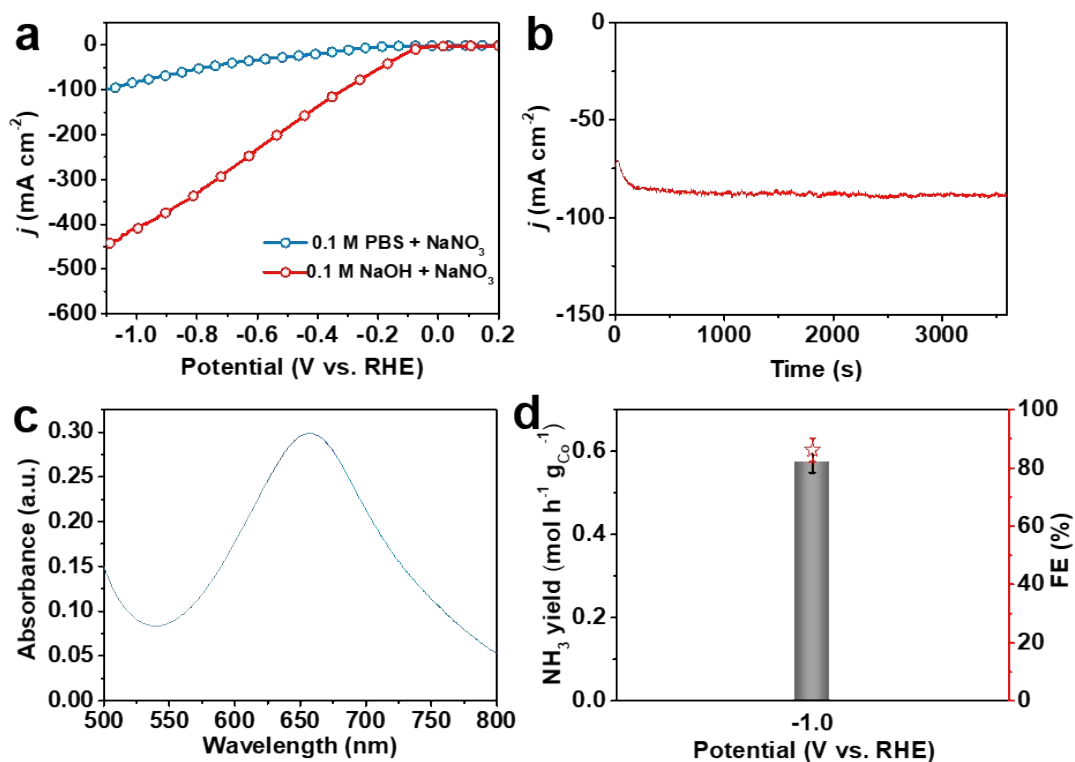


Fig. S28. (a) LSV curves of Co@JDC/GF for NO₃RR in 0.1 M PBS or 0.1 M NaOH electrolyte with 0.1 M NO₃⁻ at a scan rate of 5 mV s⁻¹ from 0.2 V to -1.1 V. (b) Chronoamperometry curve, (c) UV-Vis adsorption spectrum of electrolyte with 50 times dilution after electrolysis on Co@JDC/GF at -1.0 V in 0.1 M PBS with 0.1 M NO₃⁻ and (d) corresponding yield and FE of NH₃ for Co@JDC/GF. The error bars correspond to the standard deviations of measurements over three separately prepared samples under the same conditions.

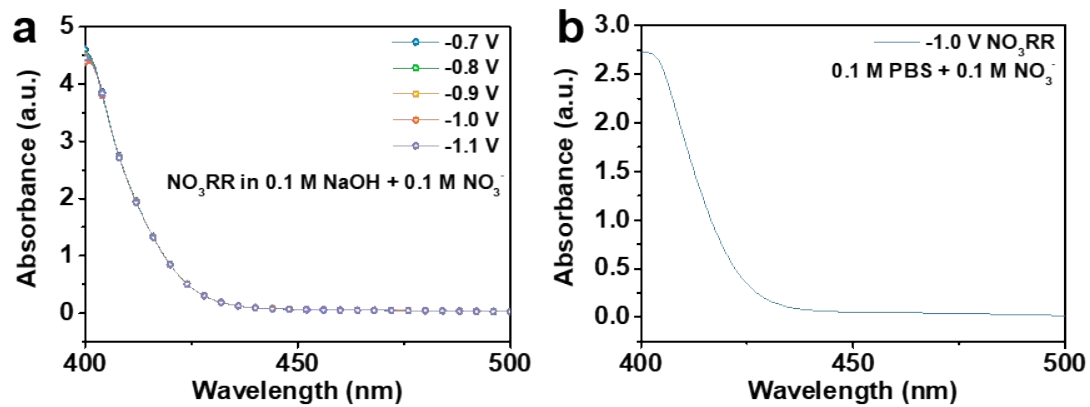


Fig. S29. (a) UV-Vis adsorption spectra of N_2H_4 in the alkaline electrolyte after electrocatalytic NO_3RR . (b) UV-Vis adsorption spectrum of N_2H_4 in the neutral electrolyte after electrocatalytic NO_3RR . There was no generation of N_2H_4 in the process of electrocatalytic NO_3RR .

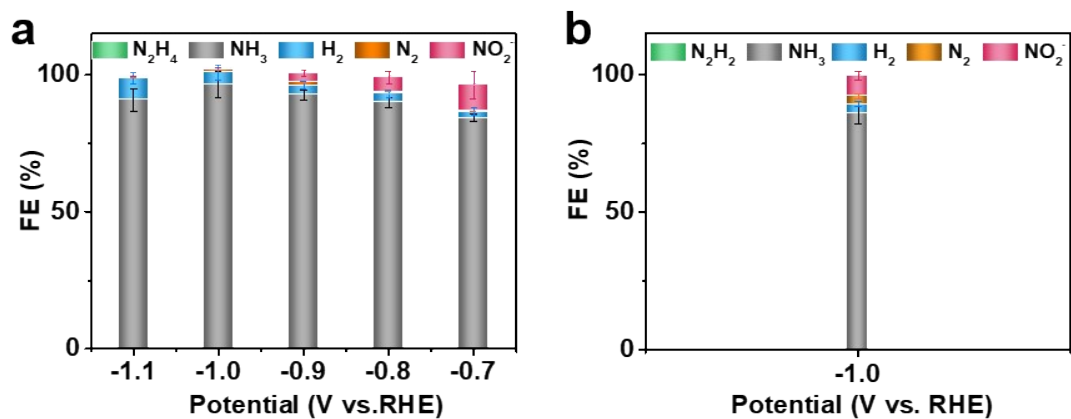


Fig. S30. (a) Product distribution for NO₃RR in the alkaline electrolyte at different potentials. (b) Product distribution for NO₃RR in the neutral electrolyte at -1.0 V. The error bars correspond to the standard deviations of measurements over three separately prepared samples under the same conditions.

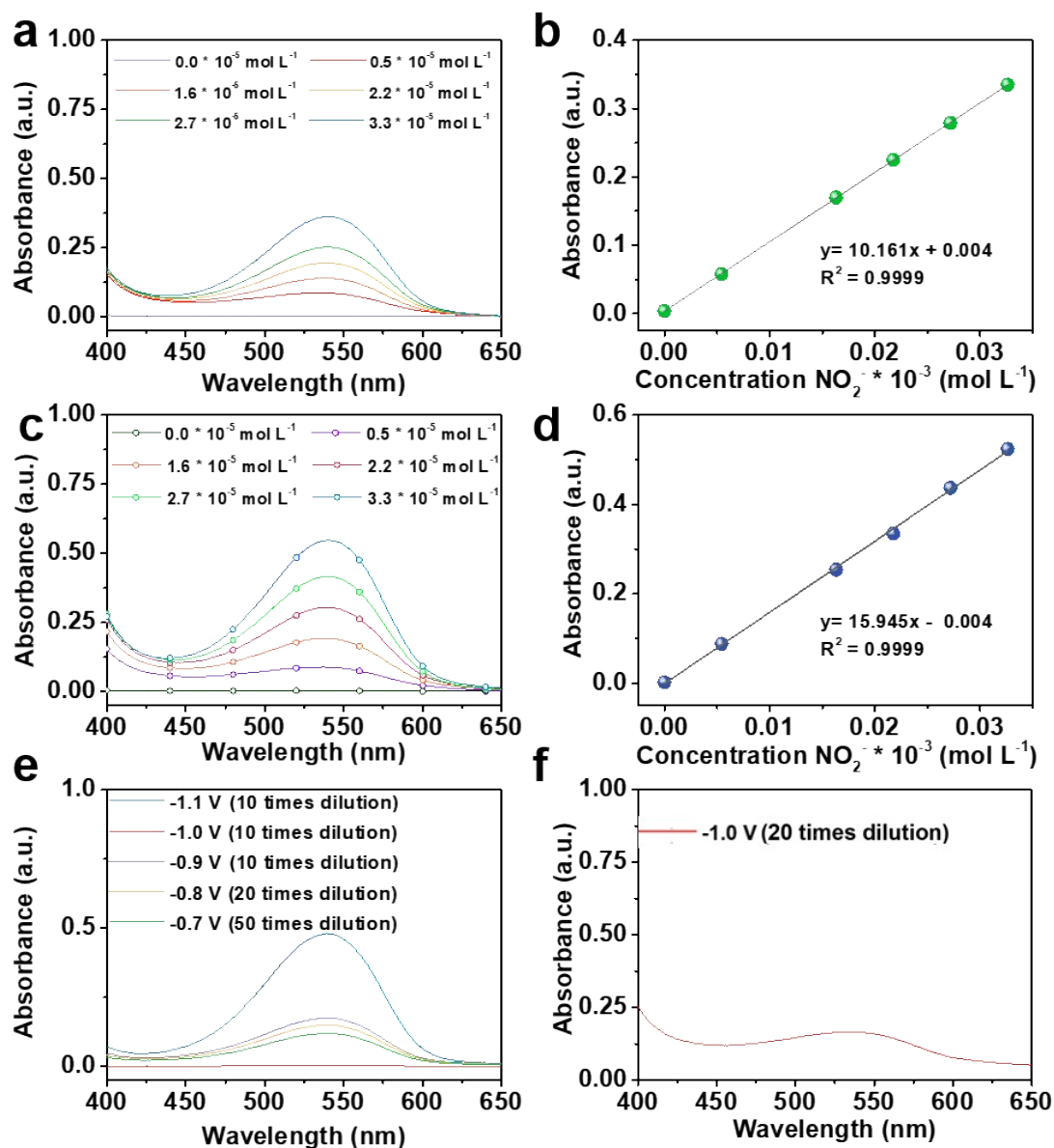


Fig. S31. (a) UV-Vis adsorption spectra of standard solution with different concentrations of NO_2^- in 0.1 M NaOH. (b) The linear standard plot to determine NO_2^- yields in 0.1 M NaOH. (c) UV-Vis adsorption spectra of standard solution with different concentrations of NO_2^- in 0.1 M PBS. (d) The linear standard plot to determine NO_2^- yields in 0.1 M PBS. (e) UV-Vis adsorption spectra of NO_2^- in the alkaline electrolyte after electrocatalytic NO_3RR at different potentials. (f) UV-Vis adsorption spectrum of NO_2^- in the neutral electrolyte after electrocatalytic NO_3RR at -1.0 V.

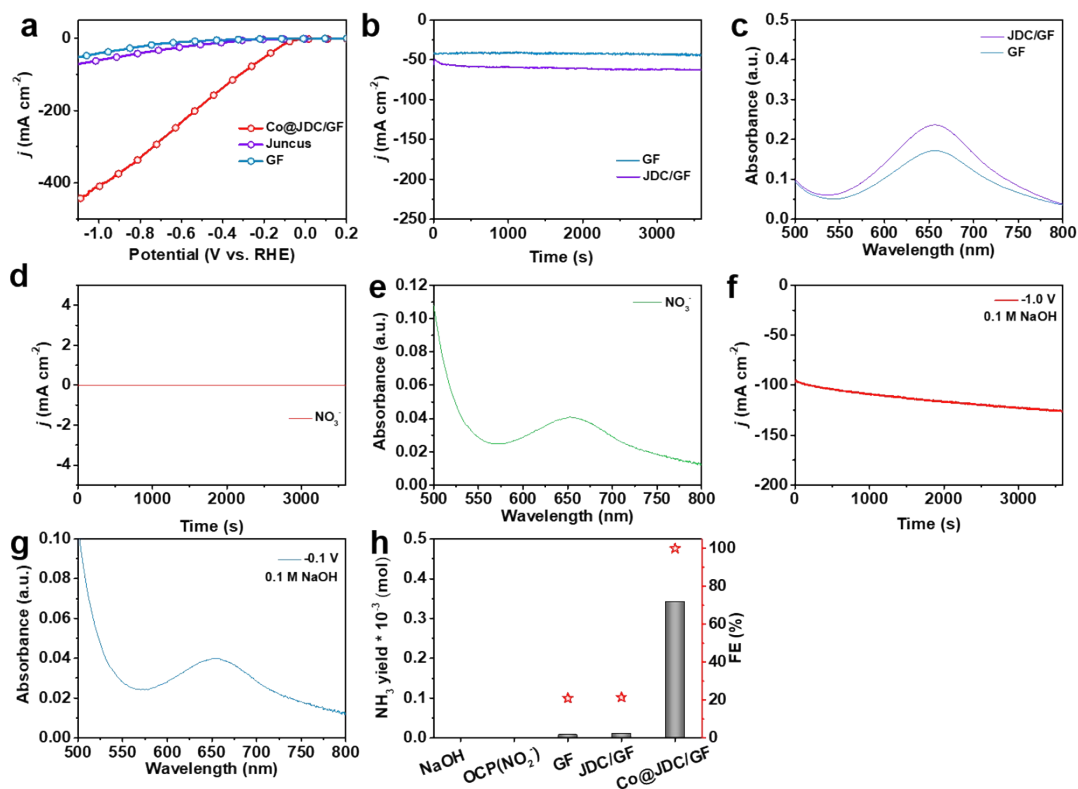


Fig. S32. (a) LSV curves of Co@JDC/GF, JDC/GF, and GF for NO₃RR in 0.1 M NaOH electrolyte with 0.1 M NO₃⁻ at a scan rate of 5 mV s⁻¹ from 0.2 V to -1.1 V. (b) Chronoamperometry curves and (c) UV-Vis adsorption spectra of the electrolytes with 10 times dilution after electrolysis on of JDC/GF and GF at -1.0 V in 0.1 M NaOH with 0.1 M NO₃⁻. (d) Chronoamperometry curve and (e) UV-Vis adsorption spectrum of electrolyte with 50 times dilution of the Co@JDC/GF at OCP in 0.1 M NaOH with 0.1 M NO₃⁻. (f) Chronoamperometry curve and (g) UV-Vis adsorption spectrum of electrolyte with 50 times dilution of the Co@JDC/GF at -1.0 V in 0.1 M NaOH. (h) Comparison of NH₃ yields after 1h electrolysis of different electrocatalysts.

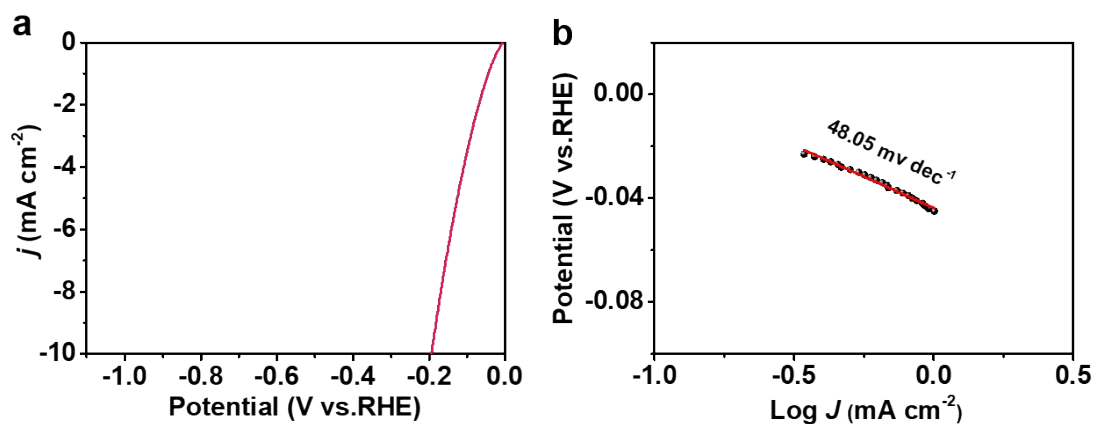


Fig. S33. (a) LSV curve for nitrate reduction on Co@JDC/GF on rotating disk electrode (RDE) at a scan rate of 5 mV s⁻¹ and rotating speed of 1600 rpm in 0.1 M NaOH with 0.1 M NO₃⁻. (b) Corresponding Tafel slope collected in the kinetic control region in (a).

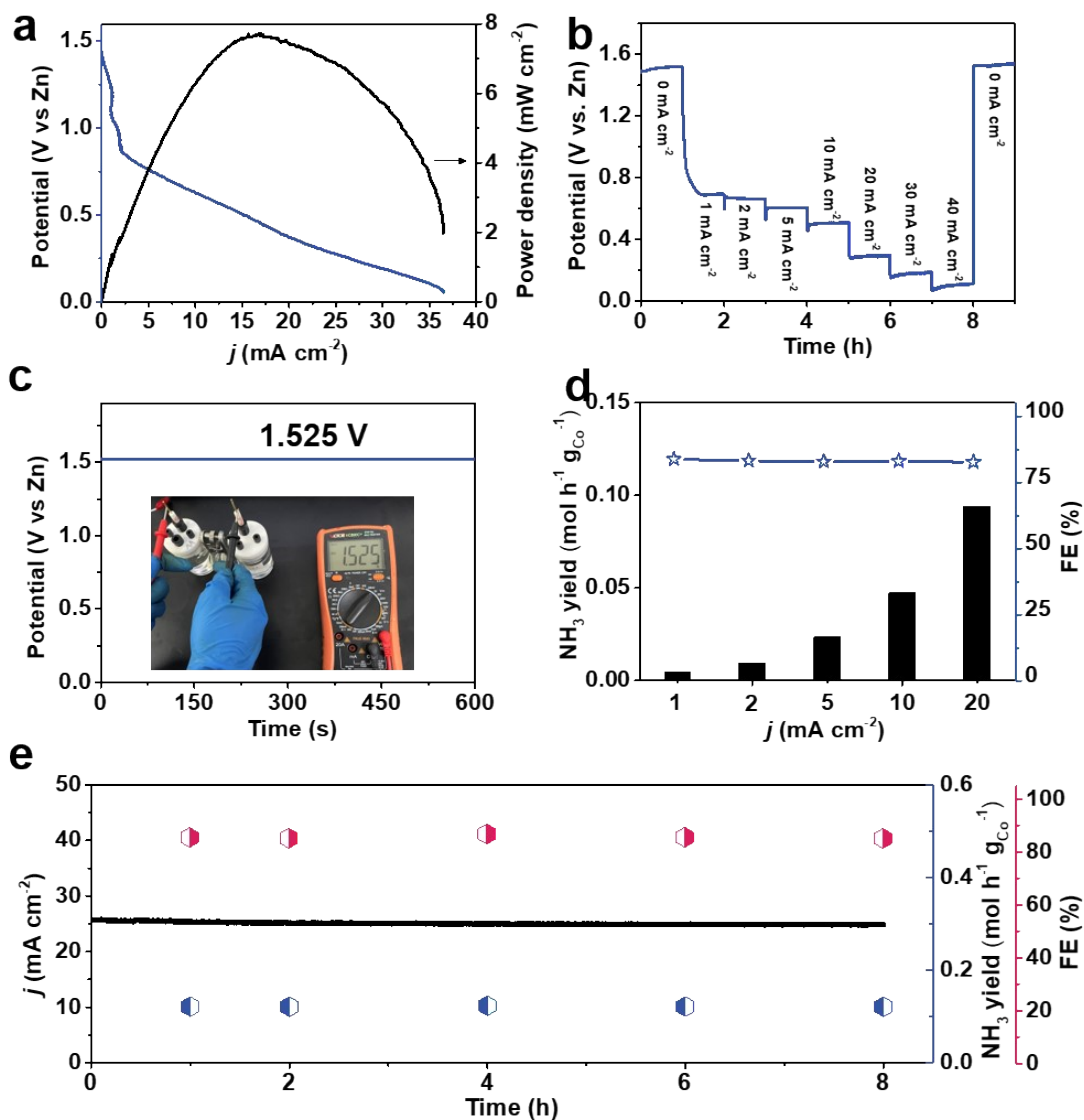


Fig. S34. (a) Polarization curves and power density of the Zn-NO₃⁻ battery with the Co@JDC/GF cathode. (b) Discharging tests at various current densities. (c) OCP of the Zn-NO₃⁻ battery. (d) NH₃ yields and the corresponding FEs. (e) Long-term stability tests.

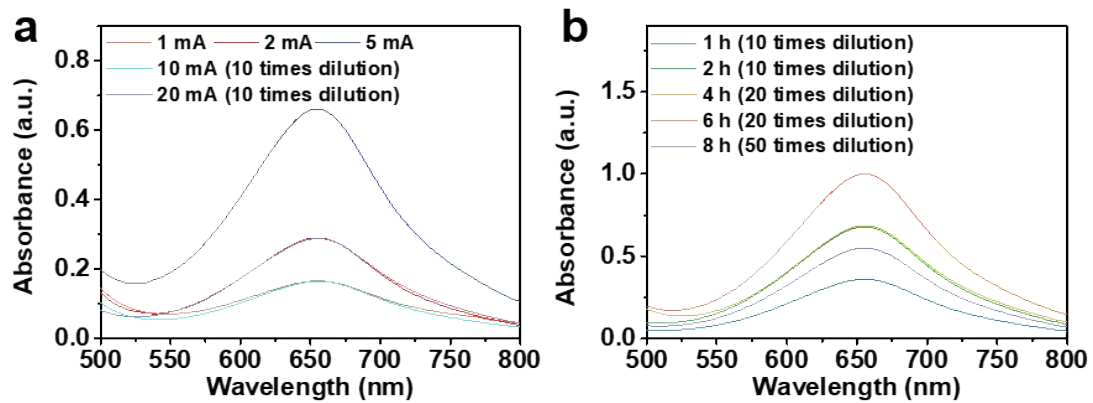


Fig. S35. (a) UV-Vis adsorption spectra of NH_3 for the Zn-NO_3^- battery system at different current densities. (b) UV-Vis adsorption spectra of NH_3 under different time periods for the Zn-NO_3^- battery system.

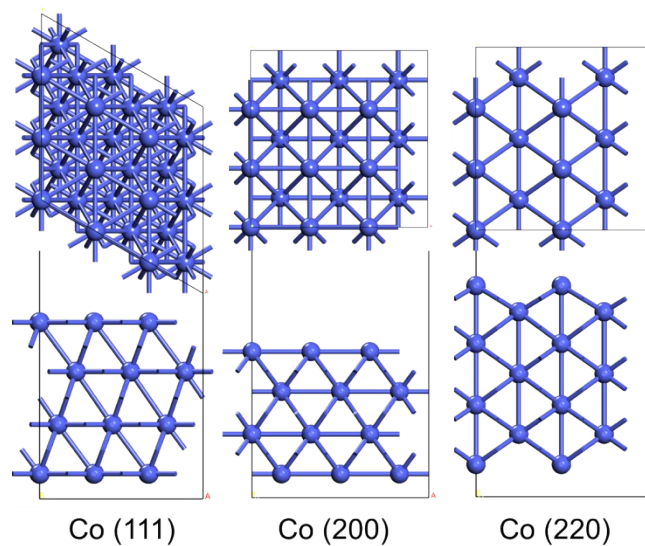


Fig. S36. Top and side view structures of Co(111), Co(200), and Co(220) surfaces, the Co atoms are shown blue.

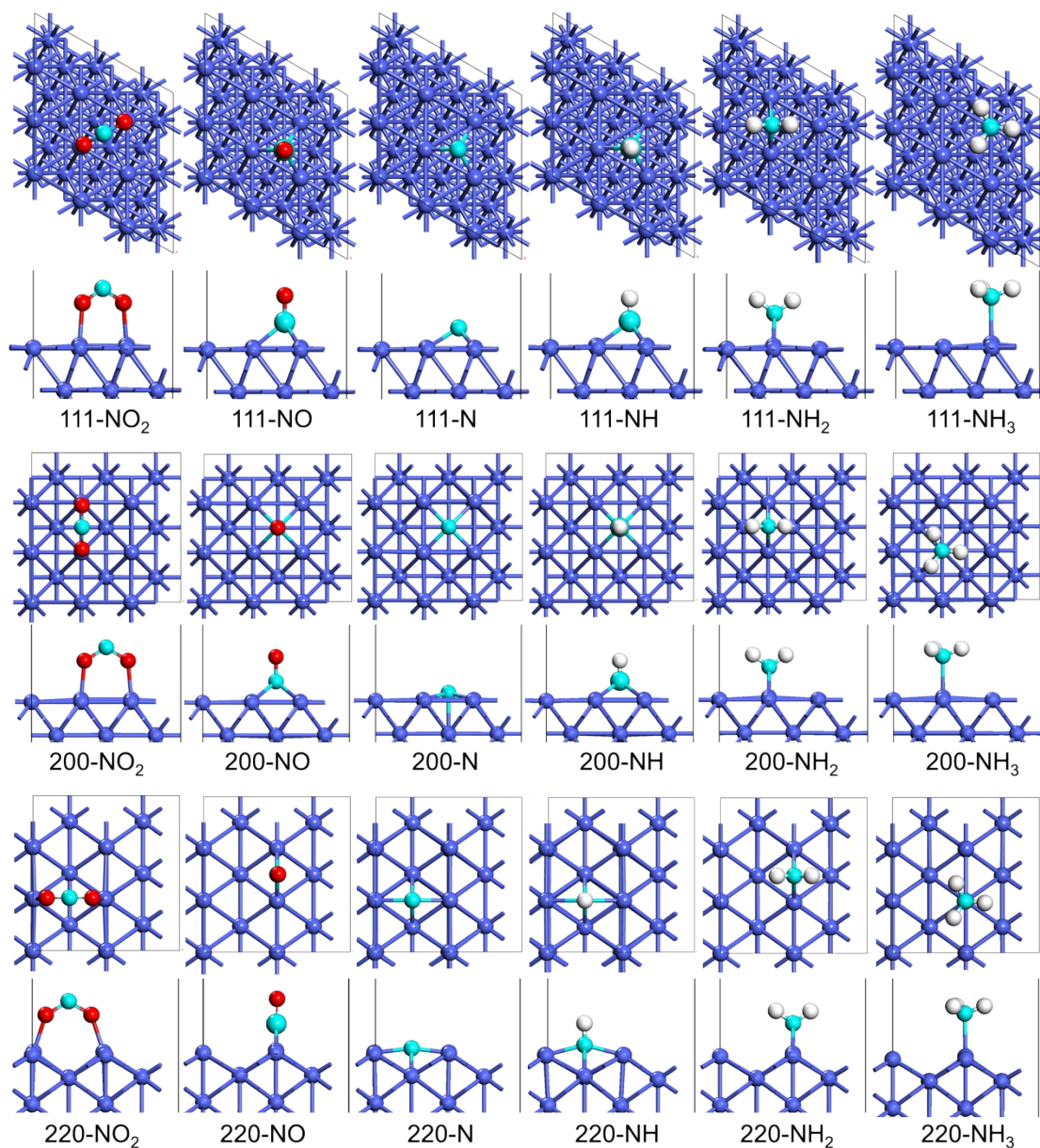


Fig. S37. Top and side view adsorption configurations of NO₂RR intermediates on Co(111), Co(200), and Co(220) surfaces, the Co, N, O, and H atoms are shown blue, cyan, red, and white, respectively.

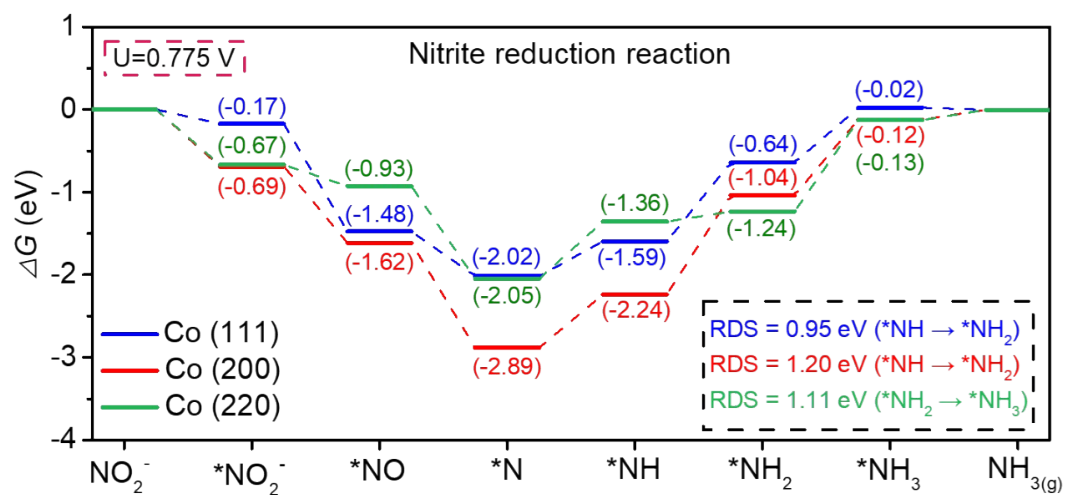


Fig. S38. Free-energy diagrams of NO_2RR on the Co(111), Co(200), and Co(220) planes at 0.775 V.

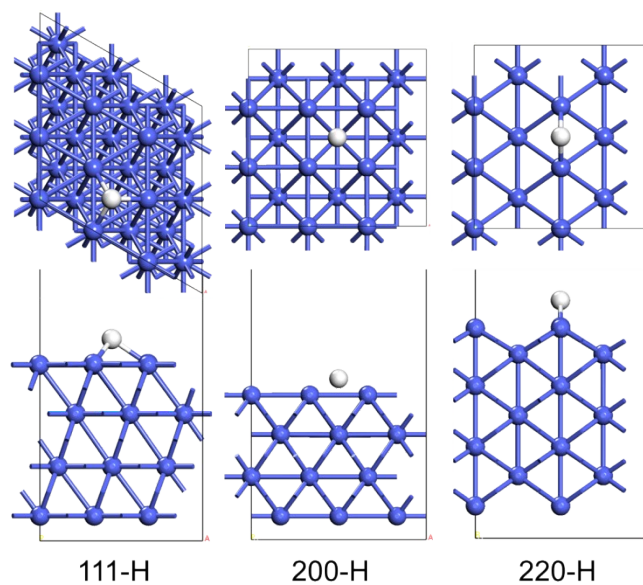


Fig. S39. Top and side view adsorption configurations of HER intermediate on Co(111), Co(200), and Co(220) surfaces, the Co, and H atoms are shown blue, and white, respectively.

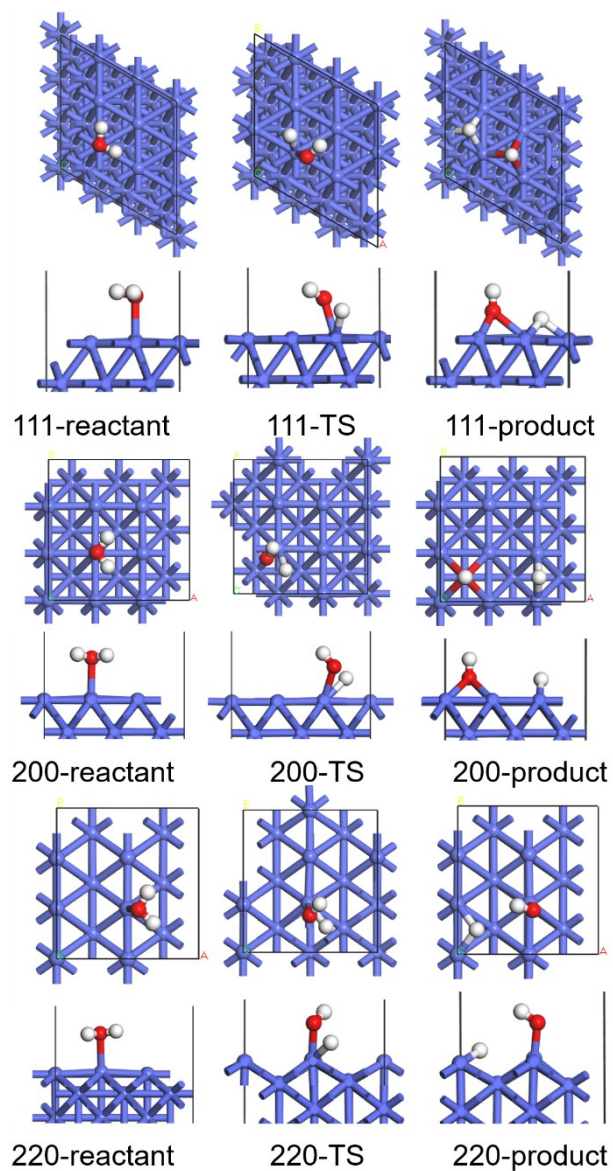


Fig. S40. Top and side view adsorption configurations of reactant initial states, intermediate state, final states and additional transition states (TS) on Co(111), Co(200), and Co(220) surfaces, the Co, and H atoms are shown blue, and white, respectively.

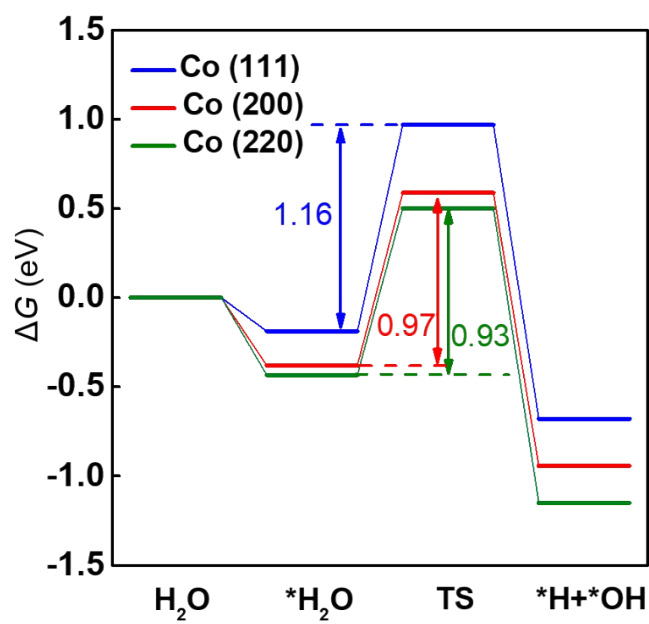


Fig. S41. Reaction free energies for intermediates on Co(111), Co(200), and Co(220) surfaces toward water dissociation kinetic of Volmer step.

Table S1. Content analysis of Co by ICP-MS.

Samples	Co (wt%)
Co@JDC-1	82.92
Co@JDC-2	83.86
Co@JDC-3	80.38
Average	82.39

Table S2. Comparing the NO₂RR performance of our synthesized Co@JDC/GF with other reported electrocatalysts.

Electrocatalyst	Electrolyte	NH ₃ yield	FE (%)	Reference
Co@JDC/GF	0.1 M PBS + 0.1 M NaNO ₂	12.71 mg h ⁻¹ cm ⁻²	90.6 ±	This work
		0.8 mol h ⁻¹ g _{Co} ⁻¹	3.1	
	0.1 M NaOH + 0.1 M NaNO ₂	40.02 mg h ⁻¹ cm ⁻²	96.9 ±	
		2.8 mol h ⁻¹ g _{Co} ⁻¹	2.1	
Ni ₃₅ /NC-sd	0.5 M Na ₂ SO ₄ + 0.3 M NaNO ₂	25.1 mg h ⁻¹ cm ⁻²	99	13
Ni-NSA-V _{Ni}	0.2 M Na ₂ SO ₄ + 200 ppm NaNO ₂	4.01 mg h ⁻¹ cm ⁻²	88.9	14
CoP NA/TM	0.1 M PBS + 500 ppm NaNO ₂	2.26 mg h ⁻¹ cm ⁻²	90	15
Ni ₂ P/NF	0.1 M PBS + 200 ppm NaNO ₂	2.69 mg h ⁻¹ cm ⁻²	90	16

Ni₃₅: high density of metallic Ni nanoparticles (35 wt%).

Table S3. Comparison of NH₃ yield and power density of our battery with reported metal-N₂, metal-NO and metal-NO₃⁻ battery systems.

Battery systems	Electrocatalyst	Power density	NH ₃ yield	Reference
metal- NO ₂ ⁻	Co@JDC/GF	10.50 mW cm ⁻²	2.9 mg h ⁻¹ cm ⁻²	This work
metal-NO	MoS ₂ /CP	1.04 mW cm ⁻²	411.8 μg h ⁻¹ cm ⁻²	15
metal-NO ₃ ⁻	Pd-doped TiO ₂ nanoarray	0.87 mW cm ⁻²	0.54 mg h ⁻¹ cm ⁻²	16
metal-NO	Ni ₂ P/CP	1.53 mW cm ⁻²	62.05 μg h ⁻¹ mg _{cat.} ⁻¹	17
metal-NO	NiO/CP	0.88 mW cm ⁻²	228 μg h ⁻¹ cm ⁻²	18

Table S4. Comparing the NO₃RR performance of our synthesized Co@JDC/GF with other reported electrocatalysts.

Electrocatalyst	Electrolyte	NH ₃ yield	FE (%)	Reference
Co@JDC/GF	0.1 M PBS + 0.1 M NaNO ₃	7.32 mg h ⁻¹ cm ⁻²	86.1 ± 4.1	This work
		0.6 mol h ⁻¹ g _{Co} ⁻¹		
	0.1 M NaOH + 0.1 M NaNO ₃	28.34 mg h ⁻¹ cm ⁻²	93.2 ± 4.8	
		2.6 mol h ⁻¹ g _{Co} ⁻¹		
Fe SAC	0.1 M K ₂ SO ₄ + 0.5 M KNO ₃	20 mg h ⁻¹ mg _{cat.} ⁻¹	75	21
In-S-G	1 M KOH + 0.1 M NaNO ₃	220 mmol h ⁻¹ g _{cat.} ⁻¹	75	22
Pd (1 1 1)	0.1 M Na ₂ SO ₄ + 0.1 M NaNO ₃	2.74 mmol h ⁻¹ mg ⁻¹	79.91	23
TiO ₂ -OVs	0.5 M Na ₂ SO ₄ + 0.1 M NaNO ₃	3.6 mmol h ⁻¹ mg ⁻¹	85	24
Cu/Cu ₂ O	0.5 M Na ₂ SO ₄ + 0.1 M NaNO ₃	5.1 mmol h ⁻¹ mg ⁻¹	95	25
Cu ₅₀ Ni ₅₀	1 M KOH + 0.1 M NaNO ₃	3.1 mmol h ⁻¹ mg ⁻¹	93± 2	26
Ru/RuO	1 M KOH + 0.1 M NaNO ₃	5.56 ± 0.18 mmol h ⁻¹ mg ⁻¹	96	27
CuO _x	0.1 M KOH + 50 ppm NaNO ₃	449.41 ± 12.18 μg h ⁻¹ mg _{cat.} ⁻¹	74.18 ± 2.27	28
Fe-PPy SACs	0.1 M KOH + 0.1 M KNO ₃	781.25 μg h ⁻¹ mg _{cat.} ⁻¹	100	29
Au/C	0.5 M K ₂ SO ₄ + 1 mM KNO ₃	407.31 μg h ⁻¹ mg ⁻¹	26	30
Cu nanosheets	0.1 M KOH + 10 mM KNO ₃	390.1 μg h ⁻¹ mg _{Cu} ⁻¹	99.7	31
Fe ₃ O ₄ /SS	0.1 M NaOH + 0.1 M NaNO ₃	82.4 ± 4.8 mg h ⁻¹ mg _{cat.} ⁻¹	93.4	32
O-Cu-PTCDA	0.1 M PBS+ 500 ppm NO ₃ ⁻ .	436 ± 85 μg h ⁻¹ cm ⁻²	85.9	33

Cu₅₀Ni₅₀: The CuNi catalysts with Cu-to-Ni ratios of 50:50 in the deposition solutions.

Fe₃O₄/SS: *in situ* grown Fe₃O₄ particle on stainless steel.

PTCDA: 3,4,9,10-perylenetetracarboxylic dianhydride.

Table S5. The adsorption energies (eV) of the intermediates in NO₂RR on the surface models of Co(111), Co(200), and Co(220).

surfaces	NO ₂	NO	N	NH	NH ₂	NH ₃
Co(111)	-1.72	-2.49	-5.51	-4.62	-2.77	-0.64
Co(200)	-2.13	-2.61	-6.36	-5.26	-3.17	-0.79
Co(220)	-2.21	-2.52	-5.62	-4.36	-3.37	-0.79

Table S6. The average inverse Bader charge of different kinds atoms in the surface models of NH-Co(111), NH-Co(200), NH₂-Co(220), NO₂-Co(111), NO₂-Co(200), and NO₂-Co(220).

surfaces	Average Inverse Bader Charge (e ⁻)			
	Co	N	O	H
NH-Co(111)	0.17	-1.15	/	0.47
NH-Co(200)	0.23	-1.24	/	0.41
NH ₂ -Co(220)	0.25	-1.28	/	0.43
NO ₂ -Co(111)	0.18	0.52	-0.58	/
NO ₂ -Co(200)	0.26	0.54	-0.62	/
NO ₂ -Co(220)	0.25	0.50	-0.60	/

Note: the inverse Bader charge is given here, which can be seen as the charge of the different atoms.

References

- (1) J. D. Genders, D. Hartsough and D. T. Hobbs, *J. Appl. Electrochem.*, 1996, **26**, 1–9.
- (2) J. G. M. Inson, C. E. Supsup and M. J. C. Flores, *Appl. Water Sci.*, 2021, **11**, 174.
- (3) Y. Liang, Y. Li, H. Wang, J. Zhou, J. Wang, T. Regier and H. Dai, *Nat. Mater.*, 2011, **10**, 780–786.
- (4) D. Zhu, L. Zhang, R. E. Ruther and R. J. Hamers, *Nat. Mater.*, 2013, **12**, 836–841.
- (5) L. C. Green, D. A. Wagner, J. Glogowski, P. L. Skipper, J. S. Wishnok and S. R. Tannenbaum, *Anal. Biochem.*, 1982, **126**, 131–138.
- (6) G. W. Watt and J. D. Chrisp, *Anal. Biochem.*, 1952, **24**, 2006–2008.
- (7) Z. Chen, T. Wang, B. Liu, D. Cheng, C. Hu, G. Zhang, W. Zhu, H. Wang, Z.-J. Zhao and J. Gong, *J. Am. Chem. Soc.*, 2020, **142**, 6878–6883.
- (8) G. Kresse and J. Furthmüller, *Comp. Mater. Sci.*, 1996, **6**, 15–50.
- (9) G. Kresse and J. Furthmüller, *Phys. Rev. B*, **54**, 11169–11186.
- (10) P. E. Blöchl, *Phys. Rev. B*, 1994, **50**, 17953–17979.
- (11) G. Kresse and D. Joubert, *Phys. Rev. B*, 1999, **59**, 1758–1775.
- (12) John P. Perdew, Kieron Burke, and Matthias Ernzerhof, *Phys. Rev. Lett.*, 1996, **77**, 3865–3868.
- (13) P. Gao, Z.-H. Xue, S.-N. Zhang, D. Xu, G.-Y. Zhai, Q.-Y. Li, J.-S. Chen and X.-H. Li, *Angew. Chem., Int. Ed.*, 2021, **60**, 20711–20716.
- (14) C. Wang, W. Zhou, Z. Sun, Y. Wang, B. Zhang and Y. Yu, *J. Mater. Chem. A*, 2021, **9**, 239–243.
- (15) G. Wen, J. Liang, Q. Liu, T. Li, X. An, F. Zhang, A. A. Alshehri, K. A. Alzahrani, Y. Luo, Q. Kong and X. Sun, *Nano Res.*, 2022, **15**, 972–977.
- (16) G. Wen, J. Liang, L. Zhang, T. Li, Q. Liu, X. An, X. Shi, Y. Liu, S. Gao, A. M. Asiri, Y. Luo, Q. Kong and X. Sun, *J. Colloid. Interf. Sci.*, 2022, **606**, 1055–1063.
- (17) L. Zhang, J. Liang, Y. Wang, T. Mou, Y. Lin, L. Yue, T. Li, Q. Liu, Y. Luo, N. Li, B. Tang, Y. Liu, S. Gao, A. A. Alshehri, X. Guo, D. Ma and X. Sun, *Angew. Chem., Int. Ed.*, 2021, **60**, 25263–25268.
- (18) Y. Guo, R. Zhang, S. Zhang, Y. Zhao, Q. Yang, Z. Huang, B. Dong and C. Zhi,

Energy Environ. Sci., 2021, **14**, 3938–3944.

- (19) T. Mou, J. Liang, Z. Ma, L. Zhang, Y. Lin, T. Li, Q. Liu, Y. Luo, Y. Liu, S. Gao, H. Zhao, A. M. Asiri, D. Ma and X. Sun, *J. Mater. Chem. A*, 2021, **9**, 24268–24275.
- (20) P. Liu, J. Liang, J. Wang, L. Zhang, J. Li, L. Yue, Y. Ren, T. Li, Y. Luo, N. Li, B. Tang, Q. Liu, A. M. Asiri, Q. Kong and X. Sun, *Chem. Commun.*, 2021, **57**, 13562–13565.
- (21) Z.-Y. Wu, M. Karamad, X. Yong, Q. Huang, D. A. Cullen, P. Zhu, C. Xia, Q. Xiao, M. Shakouri, F.-Y. Chen, J. Y. Kim, Y. Xia, K. Heck, Y. Hu, M. S. Wong, Q. Li, I. Gates, S. Siahrostami and H. Wang, *Nat. Commun.*, 2021, **12**, 2870.
- (22) F. Lei, W. Xu, J. Yu, K. Li, J. Xie, P. Hao, G. Cui and B. Tang, *Chem. Eng. J.*, 2021, **426**, 131317.
- (23) Y. Han, X. Zhang, W. Cai, H. Zhao, Y. Zhang, Y. Sun, Z. Hu, S. Li, J. Lai and L. Wang, *J. Colloid. Interf. Sci.*, 2021, **600**, 620–628.
- (24) R. Jia, Y. Wang, C. Wang, Y. Ling, Y. Yu, B. Zhang, *ACS Catal.*, 2020 **10**, 3533–3540.
- (25) Y. Wang, W. Zhou, R. Jia, Y. Yu, B. Zhang, *Angew. Chem., Int. Ed.*, 2020, **59** 5350–5354.
- (26) Y. Wang, A. Xu, Z. Wang, L. Huang, J. Li, F. Li, J. Wicks, M. Luo, D.-H. Nam, C.-S. Tan, Y. Ding, J. Wu, Y. Lum, C.-T. Dinh, D. Sinton, G. Zheng and E. H. Sargent, *J. Am. Chem. Soc.*, 2020, **142**, 5702–5708.
- (27) J. Li, G. Zhan, J. Yang, F. Quan, C. Mao, Y. Liu, B. Wang, F. Lei, L. Li, A. Chan, L. Xu, Y. Shi, Y. Du, W. Hao, P. Wong, J. Wang, S. Dou, L. Zhang, J. Yu, *J. Am. Chem. Soc.*, 2020, **142**, 7036–7046.
- (28) J. Geng, S. Ji, H. Xu, C. Zhao, S. Zhang and H. Zhang, *Inorg. Chem. Front.*, 2021, **8**, 5209–5213.
- (29) Y. Xu, M. Z. Wang, K. L. Ren, T. L. Ren, M. Y. Liu, Z. Q. Wang, X. N. Li, L. Wang and H. J. Wang, *J. Mater. Chem. A*, 2021, **9**, 16411–16417.
- (30) J. Choi, H. L. Du, C. K. Nguyen, B. H. R. Suryanto, A. N. Simonov and D. R. MacFarlane, *ACS Energy Lett.*, 2020, **5**, 2095–2097.

- (31) X. B. Fu, X. G. Zhao, X. B. Hu, K. He, Y. N. Yu, T. Li, Q. Tu, X. Qian, Q. Yue, M. R. Wasielewski and Y. J. Kang, *Appl. Mater. Today*, 2020, **19**, 100620.
- (32) X. Fan, L. Xie, J. Liang, Y. Ren, L. Zhang, L. Yue, T. Li, Y. Luo, N. Li, B. Tang, Y. Liu, S. Gao, A. A. Alshehri, Q. Liu, Q. Kong and X. Sun, *Nano Res.*, 2021, DOI: 10.1007/s12274-021-3951-5.
- (33) G.-F. Chen, Y. Yuan, H. Jiang, S.-Y. Ren, L.-X. Ding, L. Ma, T. Wu, J. Lu and H. Wang, *Nat. Energy*, 2020, **5**, 605–613.